Magnetic phase diagram of Ce_2Fe_{17}

Y. Janssen,* S. Chang, A. Kreyssig, and A. Kracher
Ames Laboratory, U.S. DOE, Ames, Iowa 50011, USA

Y. Mozharivskyj
Department of Chemistry, McMaster University, Hamilton, Ontario, Canada L8S 4M1

S. Misra
Ames Laboratory, U.S. DOE, Ames, Iowa 50011, USA
and Department of Chemistry, Iowa State University, Ames, Iowa 50011, USA

P. C. Canfield
Ames Laboratory, U.S. DOE, Ames, Iowa 50011, USA
and Department of Physics and Astronomy, Iowa State University, Ames, Iowa 50011, USA
(Received 22 December 2006; revised manuscript received 17 April 2007; published 10 August 2007)

Rare-earth-based permanent-magnet materials rich in iron have relatively low ferromagnetic ordering temperatures. This is believed to be due to the presence of antiferromagnetic exchange interactions, besides the ferromagnetic interactions responsible for the magnetic order. The magnetic properties of Ce_2Fe_{17} are anomalous. Instead of ferromagnetic, it is antiferromagnetic, and instead of one ordering temperature, it shows two, at the Néel temperature $T_N \sim 208$ K and at $T_t \sim 124$ K. Ce_2Fe_{17}, doped by 0.5% Ta, also shows two ordering temperatures, one to an antiferromagnetic phase, at $T_N \sim 214$ K, and one to a ferromagnetic phase, at $T_0 \sim 75$ K. In order to clarify this behavior, single-crystalline samples were prepared by solution growth and characterized by electron microscopy, single-crystal x-ray diffraction, temperature-dependent specific heat, and magnetic field and temperature-dependent electrical resistivity and magnetization. From these measurements, magnetic *H-T* phase diagrams were determined for both Ta-doped Ce_2Fe_{17} and undoped Ce_2Fe_{17}. These phase diagrams can be very well described in terms of a theory that gives magnetic phase diagrams of systems with competing antiferro- and ferromagnetism.

DOI: 10.1103/PhysRevB.76.054420 PACS number(s): 75.30.Kz, 64.60.Kw, 71.20.Lp, 61.50.Nw

I. INTRODUCTION

Modern permanent-magnet materials are intermetallic compounds containing rare earths (R) and transition metals, which order magnetically at temperatures much above room temperature and combine a large ferromagnetic moment with a large easy-axis magnetic anisotropy.[1] The large magnetic moment (and the high ordering temperature) is mainly provided by strongly (and ferromagnetically) coupled itinerant transition-metal magnetic moments. The strong magnetic anisotropy is mainly provided by the localized 4*f*-rare-earth magnetic moments, to which the transition-metal magnetic moments are coupled.

Because of its relative abundance in Earth's crust, Fe is the most favorable (cheapest) magnetic transition metal for use in these permanent-magnet materials. Among the rare-earth elements, Ce is most abundant, and therefore cheapest, potentially making an Fe-rich Ce-Fe compound an economical permanent-magnet material. However, the aforementioned requirements are not met. Instead, the Ce-Fe compound richest in Fe, rhombohedral Th_2Zn_{17}-type Ce_2Fe_{17}, shows abnormal[2] magnetic behavior. However, since Ce_2Fe_{17} is chemically closely related to successfully applied permanent-magnet materials,[1,3] such as $SmCo_5$ and $Nd_2Fe_{14}B$, understanding its magnetism may lead to a greater understanding of magnetism in rare-earth-transition–metal intermetallic compounds.

The R_2Fe_{17} compounds form, depending on the size of the rare-earth ion, in two different but related crystallographic structures, rhombohedral Th_2Zn_{17}-type for light (larger) rare earths and hexagonal Th_2Ni_{17}-type for heavy (smaller) rare earths.[4] Generally, they are ferromagnetic (Fe moments parallel to R-4*f* moments) for light rare earths and ferrimagnetic (Fe moments antiparallel to R-4*f* moments) for heavy rare earths.[5] Exceptions are Lu_2Fe_{17} and Ce_2Fe_{17}. These compounds have been reported to show, at least in some temperature range, antiferromagnetic behavior (see, e.g., Refs. 5–7), which for Lu_2Fe_{17} occurs between the magnetic ordering temperature (275 K) and a second critical temperature (140 K), below which it is ferromagnetic. Under a hydrostatic pressure of 0.4 GPa, Lu_2Fe_{17} remains antiferromagnetic at temperatures down to 5 K.[8]

As a representative for the magnetic behavior of the Fe magnetic subsystem in R-Fe compounds, one often considers the Y-Fe analogs (La-Fe binary intermetallic compounds do not form), and such an analog for Ce_2Fe_{17} is Y_2Fe_{17}. Y_2Fe_{17} can be prepared either with a hexagonal Th_2Ni_{17}-type or with a rhombohedral Th_2Zn_{17}-type crystal structure. Hexagonal and rhombohedral Y_2Fe_{17} are very similar in their magnetic properties, but hexagonal Y_2Fe_{17} may be easier to obtain (see, e.g., Ref. 9), while rhombohedral Y_2Fe_{17} is easier to model[10] due to its simpler crystal structure. Hexagonal Th_2Ni_{17}-type Y_2Fe_{17} is an easy-plane ferromagnet: it orders magnetically near 310 K,[5,9] and the saturated magnetic moment equals $\sim 1.95\ \mu_B$/Fe at 4.2 K. In contrast to the magnetic behavior of Co-rich Y-Co compounds, Fe-rich Y-Fe compounds have magnetic ordering temperatures that *de-*

crease with *increasing* Fe concentration, which helps put the relatively low ordering temperature of Y_2Fe_{17} in perspective (see, e.g., Ref. 3). Electronic-structure calculations indicate that Y-Fe compounds can be classified as weak ferromagnets,[10] with incomplete occupation of the majority-spin bands. For Y_2Fe_{17}, a rapid variation of the density of states near the Fermi level[10] was found. This may explain the calculated strong (and nonlinear) volume dependence of magnetization. Experimentally, hexagonal Th_2Ni_{17}-type Y_2Fe_{17} was found to have a negative thermal expansion below its magnetic ordering temperature,[11] which was phenomenologically related to strongly distance-dependent positive and negative magnetic exchange interactions between different Fe magnetic moments on different crystallographic sites, a notion that was confirmed by calculations related to electronic structure.[12] Recently, Prokhnenko *et al.*[9] found that hexagonal Y_2Fe_{17} shows antiferromagnetic behavior under sufficiently high pressures. They indicate that the magnetism in Y_2Fe_{17} under pressure may be compared to antiferromagnetism in unstable γ-Fe, which is still a challenge for electronic structure calculations.[13–16]

As determined from polycrystalline samples, Ce_2Fe_{17} orders antiferromagnetically below $T_N \sim 208$ K.[6] At 125 K, a second magnetic-order transition is observed, to another *antiferromagnetic* phase.[6,17–22] However, there are reports in which Ce_2Fe_{17} is found to be *ferromagnetic* at temperatures below an antiferroferromagnetic transition temperature,[21–24] which is sample dependent and ranges between ~20 and ~120 K.[24] It has also been reported[25] that Ce_2Fe_{17} doped with ~1.4% Si is ferromagnetic below ~120 K and antiferromagnetic between ~120 and ~210 K. Based on their Mössbauer spectroscopy experiments on different samples, nominally undoped or doped with Si or Al, from different laboratories, Hautot *et al.*[26] found that the samples which are ferromagnetic at low temperatures may be doped by small amounts of Si or by Al. Such doping may be caused by samples reacting with Al_2O_3 crucibles[3,27] or silica ampoules.

Based on the lattice constants, the unit cell of Ce_2Fe_{17} is smaller than expected from La contraction; Buschow and van Wieringen[2] deduced that Ce in Ce_2Fe_{17} is tetravalent, and therefore carries no local $4f$ moment. Later, x-ray absorption spectroscopy by Isnard *et al.*[28–30] and Vandormael *et al.*[31] indicated that Ce in Ce_2Fe_{17} is in a mixed-valent state. Furthermore, in substitutionally[30,31] and interstitially[28,29] modified Ce_2Fe_{17}, the spectroscopic Ce valence decreases with increasing Ce site volume.

Powder neutron-diffraction experiments on apparently undoped Ce_2Fe_{17} (Refs. 17 and 22) indicated that below $T_N \sim 208$ K, Ce_2Fe_{17} orders in a complex antiferromagnetic (AF) structure, which is modified below $T_t \sim 125$ K.

Magnetization experiments on polycrystalline samples hinted at a rich magnetic (H-T) phase diagram[6,19] that is strongly pressure dependent[20] and involves strong magnetovolume effects.[21] Recently, Makihara *et al.*[22] succeeded in preparing single crystals of apparently undoped Ce_2Fe_{17} that displayed anisotropic magnetization. However, a magnetic phase diagram of single-crystalline Ce_2Fe_{17} has not been determined.

Here, we report on solution-grown single crystals of Ce_2Fe_{17} and of Ta-doped Ce_2Fe_{17} and on the characterization of the crystals by magnetization, electrical transport, specific heat, x-ray diffraction, and electron-probe microanalysis. Below, we will first study the composition and the crystal structure of Ta-doped crystals and compare them to undoped crystals. Then, we present the results of extensive thermodynamic and transport measurements to determine the anisotropic H-T phase diagrams for undoped Ce_2Fe_{17}. After this, we present an H-T phase diagram obtained on a Ta-doped crystal of Ce_2Fe_{17}. Finally, the H-T phase diagrams are discussed in terms of a Moriya-Usami-type[32] theory of competing ferro- and antiferromagnetic interactions.

II. EXPERIMENT

Traditionally, R-Fe compounds are grown by self-flux out of Ta crucibles.[33,34] This technique has been used to grow Nd_2Fe_{17} as well as $Nd_2Fe_{14}B$ single crystals.[35,36] Unfortunately, as will be discussed below, Ce_2Fe_{17} allows for a slight Ta uptake[22] on one of the Fe crystallographic sites, which profoundly alters the magnetic behavior of the sample. In order to fully control the amount of Ta in the sample, we have used MgO crucibles (Ozark Technical Ceramics, Inc.), as described in Ref. 22, to grow single crystals of Ce_2Fe_{17} as well as of intentionally Ta-doped Ce_2Fe_{17}.

Starting alloys were made by arc melting pieces of Fe (99.98%, SCM Metal Products Inc., Cleveland, OH), Ce (99.9% elemental, 99.98% metal basis, Materials Preparation Center, Ames Laboratory[37]) and Ta (99.9%), in a standard arc furnace under a partial pressure of ~0.8 bar of Ti-gettered ultrahigh-purity Ar. Prior to the crystal growth experiments, the composition and temperature range for crystal growth were optimized with the aid of differential thermal analysis[27] (DTA).

The button of the starting alloy was placed in the growth crucible, a 2 ml MgO crucible. This growth crucible was capped with a strainer, a piece of Ta foil with several holes in it, while care was taken that the foil did not come in contact with the alloy to prevent possible dissolution of the Ta. On top of the capped MgO crucible, a catch crucible, an inverted 2 ml Al_2O_3 crucible, was placed. This assembly was sealed in an amorphous silica ampoule under ~0.3 bar of ultrahigh-purity argon.

To obtain undoped Ce_2Fe_{17}, an alloy with composition $Ce_{0.475}Fe_{0.525}$ was heated to 1200 °C, then allowed to equilibrate for ~2 h, quickly cooled to 1000 °C, and then cooled slowly to 940 °C, where the flux was decanted. The liquid alloy had visibly reacted with the crucible: the crucible had become brown, and on the bottom, apparently up to the level of the liquid, a brownish crust had formed. On this crust, which contained Ce oxide, we also found crystals of Ce_2Fe_{17}, which we removed mechanically. As we will see below, no Mg was found in these crystals, as may be expected from the limited solid solubility of Mg in Fe.[38]

Crystals typically grow blocky rhombohedral or tabularly, with clean and clear facets (see Fig. 1). For the tabular crystals, the facets with largest surface area were found perpendicular to the hexagonal c axis, as confirmed by x-ray diffraction. (From here, we will use hexagonal notation for the rhombohedral structure.) It appeared that the probability to

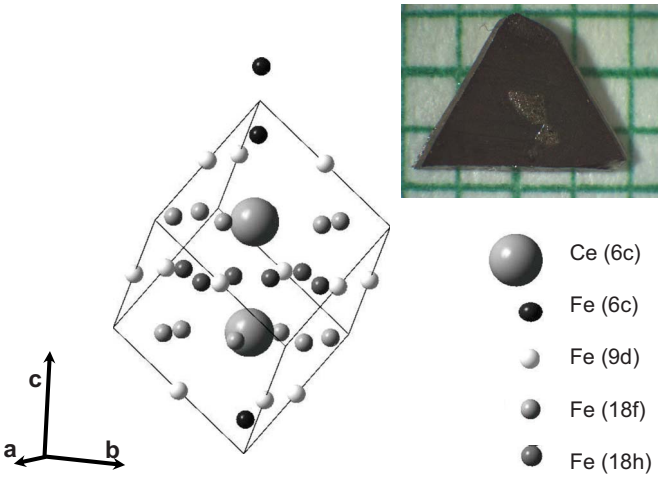

FIG. 1. (Color online) Schematic drawing (Ref. 39) of the rhombohedral unit cell of Ce_2Fe_{17}, with hexagonal axes. In Ta-doped Ce_2Fe_{17}, the Fe (6*c*) site is partially occupied by Ta. The inset shows a photograph of a platelike crystal on a millimeter-grid background. The *c* direction is perpendicular to this grid, and the sides coincide with main planar directions.

obtain tabular (or even platelike) crystals is larger when the alloy was cooled more quickly, and conversely, the probability to obtain blocky (more three-dimensional) crystals is larger when the alloy was cooled more slowly. Therefore, cooling rates varying between 0.3 and 2 °C/h were used. (Note that the DTA optimization[27] is useful here: slow cooling was performed over only 60 °C.) Among the blocky crystals, we could not find crystals longer, in the *c* direction, than ~1.5 mm. Moreover, crystals reasonably long in the *c* direction appeared to have inclusions that became visible when the crystals were cut.

Quantitative electron-probe microanalysis (EPMA) was performed with a JEOL JXA-8200 Superprobe with a 20 kV acceleration potential and a 20 nA beam current. Crystals of undoped Ce_2Fe_{17} and of Ta-doped Ce_2Fe_{17} were polished and mounted side by side. As a standard for Ce, a single crystal of the air-insensitive binary line compound $CeRu_2$ was used. For Mg, a sample of Mg_2SiO_4 was used as a standard, and for Fe and Ta, pieces of those elements were used as standards.

Single-crystal x-ray diffraction measurements were performed on the undoped and Ta-doped Ce_2Fe_{17}. Crystals with diameter of ~10 μm^3 were obtained by crushing crystals from the respective batches. Room-temperature x-ray diffraction data were collected on a STOE IPDSII image plate diffractometer with Mo $K\alpha$ radiation, and were recorded by taking 1° scans in θ in the full reciprocal sphere. 2θ ranged from 6° to 63°. Numerical absorption corrections for both crystals were based on crystal face indexing, followed by a crystal-shape optimization. Structure solution and refinement were done using the SHELXTL program.

Magnetization measurements at temperatures between 2 and 300 K in applied fields of up to 5.5 or 7 T were performed in Quantum Design MPMS-5 and MPMS-7 magnetometers, respectively, on platelike crystals as well as on blocky crystals. Zero-field ac susceptibility was measured in a Quantum Design MPMS-5 magnetometer, excitation frequency of 1000 Hz and amplitude of 0.2 mT, on a tabular crystal of ~97 mg. Specific heat was determined in a Quantum Design physical property measurement system on the same crystal as the one used for ac susceptibility. For electrical transport measurements, we used a standard four-probe technique. Bars were cut with a wire saw, both for the current *j* flowing parallel to the *c* axis and for the current *j* flowing perpendicular to the *c* axis, and electrical contact was made with Epo-tek H20E silver epoxy, with typical contact resistances of about 4 Ω. To obtain a bar for $j \perp c$ axis was relatively easy: a platelike crystal ~0.15 mm thick and several millimeters diameter was used to cut a bar of 3 mm length and 1 mm width. To obtain a good sample for $j \| c$ axis was much more difficult because of the limited available length. The resulting sample was 0.4 mm thick, 0.7 mm wide, and 1.1 mm long.

III. CHEMICAL AND STRUCTURAL CHARACTERIZATION

A total of four single-crystal samples were examined by EPMA. For one of these, the starting alloy nominally consisted only of Ce and Fe, and for the other three, the starting alloy was doped with Ta (by 0.05%, 0.5%, and 1%). The nominally undoped sample was very carefully checked for both Mg and for Ta by performing slow wavelength-dispersive spectroscopy scans over the Mg *K* and Ta *L* lines, respectively, on the standards as well as on the sample. The spectra from the nominally undoped sample showed no discernible Mg or Ta peaks. Spectra from Ta-doped samples did produce Ta peaks, and Ta-peak heights obtained by scanning were consistent with Ta-peak heights obtained by a three-point analysis. The analysis indicated that the undoped sample contained less than ~300 ppm Mg and less than ~300 ppm Ta. Quantitatively, the composition of the undoped sample was found equal to $Ce_2Fe_{16.9(1)}$. The nominally 0.05%, 0.5%, and 1% Ta-doped samples were found to contain 0.42(5)%, 0.37(5)%, and 0.57(4)% Ta, respectively, which indicates that there is a solid-solubility maximum for Ta in Ce_2Fe_{17}. Quantitatively, the compositions were found equal to $Ce_2Fe_{17.1(2)}Ta_{0.08(1)}$, $Ce_2Fe_{17.0(1)}Ta_{0.07(1)}$, and $Ce_2Fe_{17.00(9)}Ta_{0.108(7)}$ for nominally 0.05%, 0.5%, and 1% Ta, respectively. Note that these compositions do not differ significantly, i.e., by more than two standard deviations, from (2-17) stoichiometry. EPMA also indicated that samples may have parasitic inclusions of $CeFe_2$, which was also noted in Ref. 21.

An undoped crystal and the EPMA crystal, grown out of the nominally 0.05% Ta-doped alloy, were used for single-crystal x-ray diffraction experiments. The crystallographic and structural data are summarized in Tables I and II for undoped and Ta-doped Ce_2Fe_{17}, respectively. We refined the x-ray diffraction data for the undoped sample assuming that only Ce and Fe form the structure. The diffraction data indicate that the crystal has the rhombohedral Th_2Zn_{17}-type crystal structure with space group $R\bar{3}m$, as shown in Fig. 1, with a full occupancy of all available sites. The high quality of the

TABLE I. Atomic coordinates and equivalent isotropic displacement parameters (Å^2) for Ce_2Fe_{17}. U_{eq} is defined as one-third of the trace of the orthogonal U^{ij} tensor. Space group $R\bar{3}m$, $a=8.4890(12)$ Å, $c=12.410(4)$ Å, $R=0.0149$, and $R_w=0.0361$.

Atom (site)	x/a	y/b	z/c	Occ.	U_{eq}
Ce(6*c*)	0	0	0.34351(3)	1	0.0077(2)
Fe(6*c*)	0	0	0.09682(8)	1	0.0074(3)
Fe(9*d*)	$\frac{1}{2}$	0	$\frac{1}{2}$	1	0.0067(2)
Fe(18*f*)	0.29050(8)	0	0	1	0.0086(2)
Fe(18*h*)	0.50150(4)	0.49850(4)	0.15502(5)	1	0.0078(2)

refinement (the refinement factor $R=0.0149$) indicates that this crystal has no obverse-reverse twins (reticular merohedry), as found for the related compound Pr_2Fe_{17} (see Ref. 40). We found for the lattice parameters of the undoped Ce_2Fe_{17} crystal $a=8.4890(12)$ Å and $c=12.410(4)$ Å. These unit-cell parameters agree very well with those found for apparently undoped Ce_2Fe_{17} (see Ref. 21). The atomic position parameters, see Table I, are in good agreement with published values.[41]

Although it was clear from the EPMA experiments that there was Ta in the doped sample, we initially refined the diffraction data from this crystal assuming that only Ce and Fe form the structure. Although in this case the *R* factor was only slightly higher than the *R* factor for the final refinement shown in Table II, 0.0504 instead of 0.0496, the refined isotropic displacement parameter for the Fe-6*c* site became very small, 0.0021(6) instead of 0.0074(11). This value is much lower than the displacement parameters found for the other Fe atoms in the structure, whereas for pure Ce_2Fe_{17}, Table I, values were about equal for the different Fe sites. Since small thermal displacements have the same effect on diffracted beam intensities as larger electron densities, it appears that the electron density on the Fe-6*c* site is too low in the model, without Ta. The introduction of an Fe/Ta mixture on the Fe-6*c* site brings the temperature factor to the level of the other Fe atoms. Further refinements, allowing for mixtures on the other crystallographic sites, made clear that Ta has a strong preference to substitute for Fe on this Fe-6*c* site. Therefore, the structure was refined with Ta only on that site. The final refinement factor $R=0.0496$ indicates a good fit. Residual electron density not described by the current structural model does not lead to Ta occupying possible interstitial sites by more than about 0.5%. The refined amount of Ta leads to an empirical x-ray formula of $Ce_2Fe_{16.91(2)}Ta_{0.09(2)}$ which is, within experimental error, the same as the composition found by the EPMA experiment for this crystal, $Ce_2Fe_{17.1(2)}Ta_{0.08(1)}$.

The lattice parameters and unit-cell parameters for the Ta-doped Ce_2Fe_{17} crystal [space group $R\bar{3}m$, $a=8.4972(12)$ Å, $c=12.447(3)$ Å] are slightly larger than the lattice parameters for the undoped crystal, which is consistent with reported[21] lattice parameters for Ta-crucible grown Ce_2Fe_{17}.

The result that Ta substitutes for Fe on the Fe-6*c* site is consistent with expectations, and the result that Ta has a solid-solubility maximum in Ce_2Fe_{17} is both consistent with expectations and plausible. All transition metals with a radius larger than that of Fe, which include Ta (Ref. 42), prefer to substitute for Fe on the Fe-6*c* site[43] in Nd_2Fe_{17} with the same crystal structure as Ce_2Fe_{17}. The solid solubility of Ta in isostructural Sm_2Fe_{17} has[44] a maximum of 2.3 at. % of Ta in $Sm_2Fe_{17-x}Ta_x$. In solution growth,[27,33,34] the composition of the product (crystals) is different from the composition of the initial melt (crystals plus solvent). Here, the mass ratio (yield) of crystals to flux was typically about 10%, which makes it theoretically possible to obtain crystals with as high as 0.5 at. % Ta for an initial melt with 0.05 at. % Ta.

The three Ta-doped crystals under investigation are all doped by about 0.5% Ta, which indicates that there exists, besides a limited solid solubility of Ta in Ce_2Fe_{17}, a mechanism that favors Ta to dope the crystals (Ce_2Fe_{17}) rather than remain in the solvent ($\sim Ce_{0.5}Fe_{0.5}$). This mechanism might be related to the limited solubility of Ta in liquid Ce ($\sim 0.005\%$ at ~ 1000 °C) (see Ref. 45).

TABLE II. Atomic coordinates and equivalent isotropic displacement parameters (Å^2) for Ta-doped Ce_2Fe_{17}. U_{eq} is defined as one-third of the trace of the orthogonal U^{ij} tensor. Space group $R\bar{3}m$, $a=8.4972(12)$ Å, $c=12.447(3)$ Å, $R=0.0496$, and $R_w=0.0535$.

Atom (site)	x/a	y/b	z/c	Occ.	U_{eq}
Ce(6*c*)	0	0	0.3436(1)	1	0.0068(3)
Fe(6*c*)	0	0	0.0965(2)	0.954(9)	0.0074(11)
Ta(6*c*)	0	0	0.0965(2)	0.046(9)	0.0074(11)
Fe(9*d*)	$\frac{1}{2}$	0	$\frac{1}{2}$	1	0.0060(5)
Fe(18*f*)	0.2915(2)	0	0	1	0.0071(4)
Fe(18*h*)	0.5012(1)	0.4988(1)	0.1549(1)	1	0.0080(4)

IV. PURE Ce_2Fe_{17}: ZERO-FIELD RESULTS

Temperature-dependent specific heat of Ce_2Fe_{17} is presented in Fig. 2(a). Two λ-type peaks, at 124 and at 209 K, are clearly seen. These peaks are consistent with magnetic ordering transitions found earlier in polycrystalline samples.[6]

Results of anisotropic zero-field ac-susceptibility measurements for both $H_{ac} \perp c$ axis and $H_{ac} \| c$ axis are presented in Fig. 2(c). For both ac-field directions, three features characterize the data: a sharp rise near 225 K and two weaker anomalies near 208 and 125 K, respectively. The temperature of the sharp rise, ~225 K, is consistent with the ferromagnetic ordering temperature of ~230 K of $CeFe_2$.[2] (Inclusions of $CeFe_2$ were observed in samples used for EPMA, see above.) Moreover, the sample used for the ac susceptibility presented here was the same as the one used for the specific heat experiments described above. In that experiment, no anomaly was observed near 225 K. From a magnetization isotherm measured at 5 K (not shown), we estimate the amount of $CeFe_2$ in this sample as less than 0.5%. As for the other two anomalies, they occur at temperatures near the temperatures of the peaks in specific heat, and are consistent with the previously reported ordering temperatures for Ce_2Fe_{17}.

Results of zero-field resistivity measurements are presented in Fig. 2(c). Because of the small dimensions of the samples, the estimated error in the determination of the resistivity was relatively large, about 20%. At room temperature, above the magnetic phase-transition temperatures, overlapping values were found for $j \| c$ axis and for $j \perp c$ axis, 150(30) and 190(38) $\mu\Omega$ cm, respectively. Because of this overlap, the existence of anisotropy in the resistivity at room temperature is not clear. To further study possible anisotropic temperature dependence, the resistivity results were normalized to the 300 K values.

In polycrystalline samples, resistivity anomalies associated with the magnetic ordering near 209 K were either not observed[6,18,31] or showed as a weak anomaly.[46] Here, above 220 K, the behavior of the resistivity appears indistinguishable for both employed current directions. Below that temperature, thus near 209 K, the temperature of the highest-temperature transition found in specific heat, the normalized zero-field resistivity for $j \perp c$ axis is lower than for $j \| c$ axis. Thus, near the magnetic ordering temperature, the resistivity behavior becomes anisotropic. Both curves appear approximately linear with temperature between ~130 and ~190 K.

At a still lower temperature of ~124 K, consistent with the λ-type peak in specific heat, an anomalous increase of the resistivity occurs, for both current directions, similar to the resistivity behavior below the ordering temperatures of heavy rare earths such as Er or Tm (see, e.g., Refs. 47 and 48, respectively). Such an increase, though much less pronounced, was observed earlier in polycrystalline Ce_2Fe_{17}.[6,18] The increase is much larger for $j \| c$ axis than for $j \perp c$ axis. This is consistent with the formation of anisotropic superzone gaps, gapping parts of the Fermi surface, particularly $\perp c$ axis.

We estimate the gapped fraction of the Fermi surface by considering the conductivity[49]

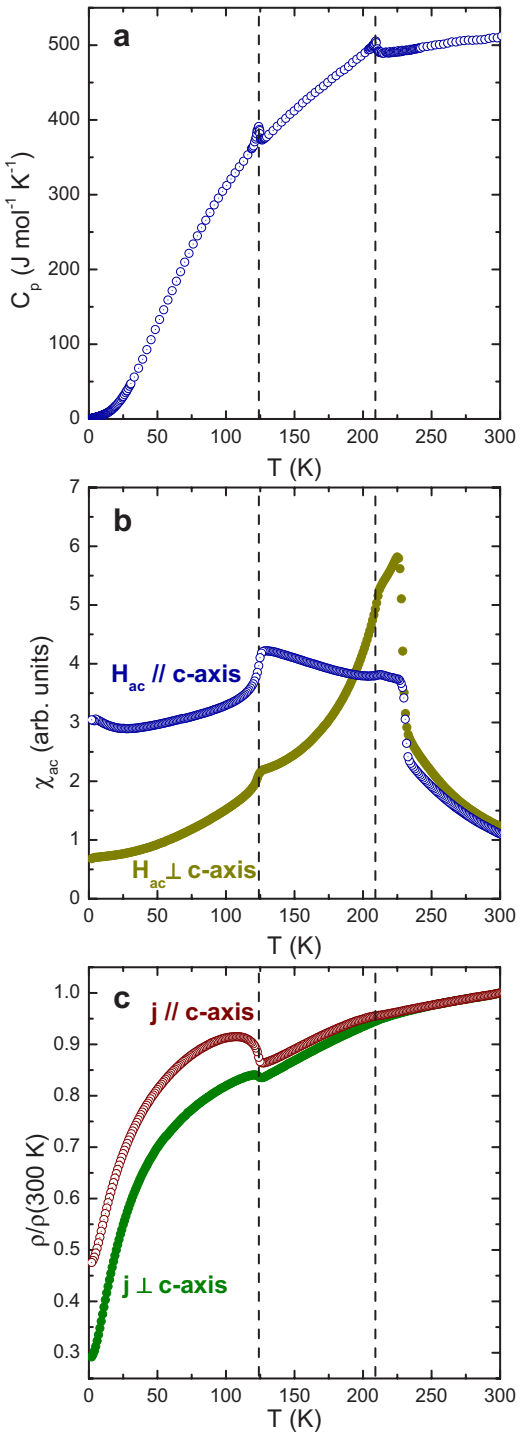

FIG. 2. (Color online) (a) Zero-field specific heat C_p as a function of temperature. The λ-type peaks, at $T_t = 124(1)$ K and $T_N = 209(2)$ K, are due to phase transitions, as described in the text. (b) ac susceptibility for the ac field applied both $\perp c$ axis and $\| c$ axis. The sharp rise, in both curves, near 230 K is due to parasitic $CeFe_2$. The dashed lines indicate the temperatures where peaks were found in the specific heat. (c) Normalized temperature-dependent zero-field resistivity $\rho(T)$ for the current flowing parallel to the c axis (open circles) and for the current flowing perpendicular to the c axis (closed circles). The dashed lines indicate the temperatures where peaks were found in the specific heat.

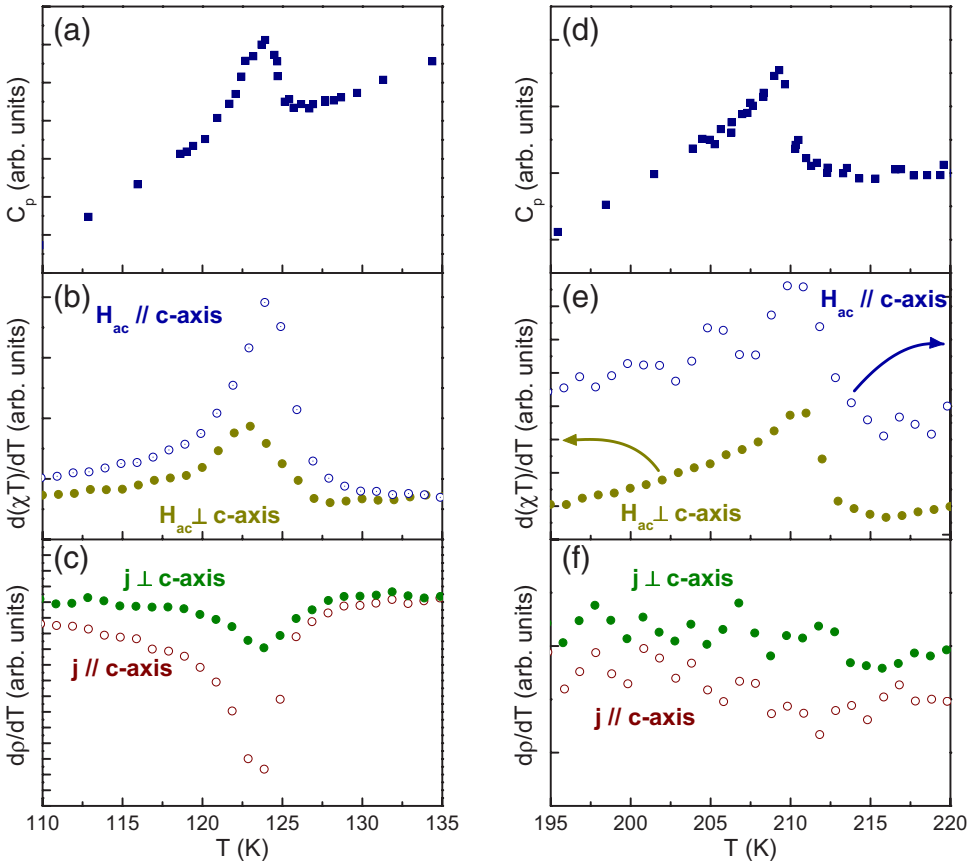

FIG. 3. (Color online) Left: (a) Specific heat, (b) $\partial(\chi T)/\partial T$ for $H_{ac} \perp c$ axis (closed circles) and for $H_{ac} \| c$ axis (open circles), and (c) $\partial\rho/\partial T$ for the current $j \| c$ axis (open circles) and for $j \perp c$ axis (closed circles), between 110 and 135 K. Right: (d) Specific heat, (e) $\partial(\chi T)/\partial T$ for $H_{ac} \perp c$ axis (closed circles) and for $H_{ac} \| c$ axis (open circles), and (f) $\partial\rho/\partial T$ for the current $j \| c$ axis (open circles) and for $j \perp c$ axis (closed circles), between 195 and 220 K.

$$\sigma = \frac{e^2}{12\pi^3\hbar} \int \Lambda dS_F, \tag{1}$$

with Λ the electron mean free path, and the integral over the Fermi surface area S_F. Assuming that Λ does not change anomalously due to the transition, the gapped fraction of the Fermi surface is proportional to the relative reduction δ in conductivity σ. If we further assume that all parts of the Fermi surface contribute equally to conductivity, the gapped fraction is equal to the relative reduction in conductivity.

Then, the assumed resistivity without superzone gaps, ρ_{without}, just below 125 K, follows the apparently linear behavior observed above 125 K. This resistivity without superzone gaps below 125 K is obtained by linear extrapolation of the resistivity between ~130 and 180 K. An estimate for δ is obtained from Eq. (1),

$$\delta = 1 - \frac{\rho_{\text{without}}}{\rho_{\text{with}}}. \tag{2}$$

The reduced resistivity for $j \| c$ axis shows a maximum near 107 K, and we assume for our estimate that the gaps have fully developed there. The reduced resistivity at 107 K reads $\rho_{\text{with,red}}=0.92$, and the extrapolated reduced resistivity reads $\rho_{\text{without,red}}=0.83$. Therefore, we estimate that the conductivity for $j \| c$ axis is reduced by $\delta \sim 10\%$ due to the superzone gaps. Obtained in a similar manner, we estimate that the conductivity for $j \perp c$ axis is reduced by ~3%. This anisotropic behavior is consistent with expectations due to the reported propagation vectors for the magnetic structure, parallel to the c axis.[11,22,50]

Furthermore, the zero-field resistivity for both current directions shows a rather small residual resistance ratio (RRR), about 2 for $j \| c$ axis and about 3 for $j \perp c$ axis. Such values may indicate poor sample quality, however, in an applied field RRR is much larger for both current directions, as will be shown below; we think that in Ce_2Fe_{17} a strong magnetic scattering is the major cause for such low RRR values.

As already indicated above, in the measurements of specific heat, ac susceptibility, and resistivity, the two ordering temperatures are observed. Anomalies in $\frac{\partial\rho}{\partial T}$ coinciding with specific heat anomalies are frequently observed in magnetic materials (see, e.g., Refs. 51–53). For an accurate phase-diagram determination to be described in the next sections, criteria for determining transition temperatures are needed. In Fig. 3, we present temperature-dependent specific heat (a) between 110 and 135 K, compared to $\frac{\partial(\chi T)}{\partial T}$ (b) and $\frac{\partial\rho}{\partial T}$ for both current directions (c). There is good agreement between the specific heat and $\frac{\partial(\chi T)}{\partial T}$ (b) even though, strictly, the theories in Refs. 54 and 55 are only good for paramagnetic to

antiferromagnetic transitions. Clear anomalies, with (besides the fact that they point downward) similar shapes as the peak in specific heat, are also observed in $\frac{\partial \rho}{\partial T}$ (c) for both current-flow directions.

In Fig. 3, we also present temperature-dependent specific heat (d) between 195 and 230 K, compared to $\frac{\partial(\chi T)}{\partial T}$ for both ac-field directions (e) and $\frac{\partial \rho}{\partial T}$ for both current directions (f). Aside from the sharp downturn above ~224 K [see Fig. 2(b)], which we ascribed to an impurity of $CeFe_2$, there is good agreement between the specific heat (d) and $\frac{\partial(\chi T)}{\partial T}$ for $H \perp c$ axis and reasonable agreement for $H \| c$ axis (e). Such an agreement is expected for simple antiferromagnets as well as for less-simple antiferromagnets, see Refs. 54 and 55, respectively. As expected from the absence of a clear anomaly in the individual resistivity curves for both $j \| c$ axis and $j \perp c$ axis, see Fig. 2(c), a clear anomaly is not observed in $\frac{\partial \rho}{\partial T}$ (f) for either current-flow direction.

Ideally, phase transitions are determined by specific heat. These measurements, however, are time consuming and may be hindered by torque and, as will be described below, by sample fragility. Therefore, for the determination of phase-transition fields and temperatures, we made use of magnetization and electrical resistivity data. Above, we found that Ce_2Fe_{17} anomalies in the specific heat C_p are also found in susceptibility via Fisher's relation[54] $\frac{\partial(\chi T)}{\partial T}$ and in the resistivity via $\frac{\partial \rho}{\partial T}$. Below, we will make use of a modified version of Fisher's relation, $\frac{\partial(MT)}{\partial T}$, and verify some of the results with $\frac{\partial \rho}{\partial T}$ from resistivity measurements, as well as with transition fields obtained from anomalies in $\frac{\partial M}{\partial H}$ obtained from magnetization isotherms.[56]

V. PURE Ce_2Fe_{17}: RESULTS FOR $H \perp c$ AXIS

A. Magnetization

We did not observe any noticeable differences in magnetization for fields applied in different directions within the plane $\perp c$ axis; therefore, they will be presented as measured with $H \perp c$ axis. Before we discuss these experiments, we address the fragility of the compound. It has been reported[21] that at ~5 K, the crystallographic unit-cell volume is larger in 5 T than in zero field by ~0.7%. At 1.8 K, a hysteretic metamagnetic transition, see below, takes place, presumably from a low-field, small-volume phase to a high-field, larger-volume phase. In a magnetization experiment, at 1.8 K, on a platelike sample, the sample *shattered* while the magnetic field ($H \perp c$ axis) *decreased* through this transition.

Although the data from the two types of crystal overlap, we found platelike samples to behave differently from blocky samples. On blocky samples, we have been able to measure full-hysteresis magnetization isotherms at temperatures between 1.8 and 300 K. Visual inspection after the measurements revealed no obvious damage.

The platelike samples, with their surface normal parallel to the c axis, were easy to (re)align, within 2°–3°, and easier to clamp than the blocky samples. Because of their relative ease of use, we chose the platelike samples for the detailed magnetization measurements and developed a protocol that helps circumvent their fragility. For determining hysteresis behavior, we used blocky samples.

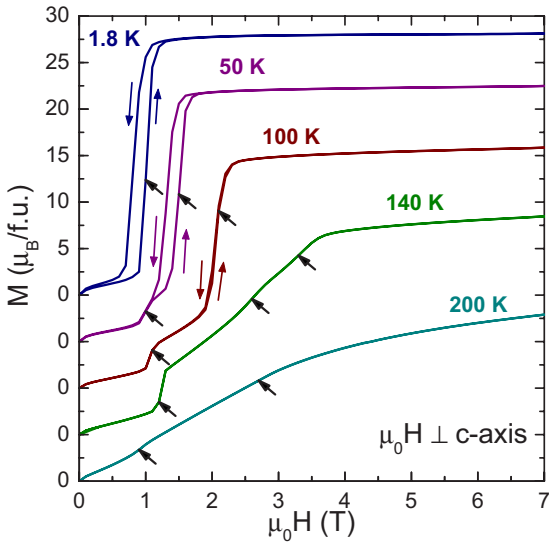

FIG. 4. (Color online) Magnetization at various temperatures for Ce_2Fe_{17} with the magnetic field $\mu_0 H \perp c$ axis, measured with increasing and decreasing fields with steps of 0.1 T. For clarity, the curves have been offset with respect to one another. The black arrows indicate maxima in $\frac{\partial M}{\partial H}$ for increasing fields.

Figure 4 shows magnetization at various temperatures, measured on a blocky sample with both increasing and decreasing field strengths up to 7 T, applied $\perp$ the c axis, with a step of 0.1 T between measurements. With increasing fields, the magnetization at 1.8 K is small and increases only slightly in fields up to ~1 T. Then, around ~1 T, the magnetization jumps to saturation and is nearly field independent, reaching ~27 μ_B/f.u. at 7 T. This jump in magnetization shows a hysteresis of about 0.2 T. The magnetization at 50 and 100 K also shows hysteretic jumps to saturation, at ~1.5 and ~2.1 T, respectively. The width of the hysteresis becomes smaller with increasing temperature. Besides the hysteretic metamagnetic transition in high fields, the curves measured at 50 and 100 K both also show a steplike feature near 1 T with no detectable hysteresis, indicative of another metamagnetic transition.

At temperatures above ~125 K, the lower zero-field transition temperature described in the previous section, magnetization isotherms are qualitatively different. At 140 K, besides a step in magnetization that occurs here at ~1.2 T, the magnetization follows an s-shape increase with increasing fields with a bending point near 2.6 T, up to ~3.3 T, where the magnetization starts to saturate. Hysteresis is not observed. At 200 K, still in the magnetically ordered phase, a weak feature is observed near ~0.9 T, and a change in slope may be discerned near ~2.7 T, indicating that the magnetization starts to saturate above this field strength.

Figure 5 shows the field evolution of temperature-dependent magnetization, measured on a platelike sample, at temperatures between 240 and 80 K. In a field of 4.25 T, the magnetization increases monotonically with decreasing temperatures, without any clear anomalies. In lower fields, multiple anomalies occur, associated with magnetic phase tran-

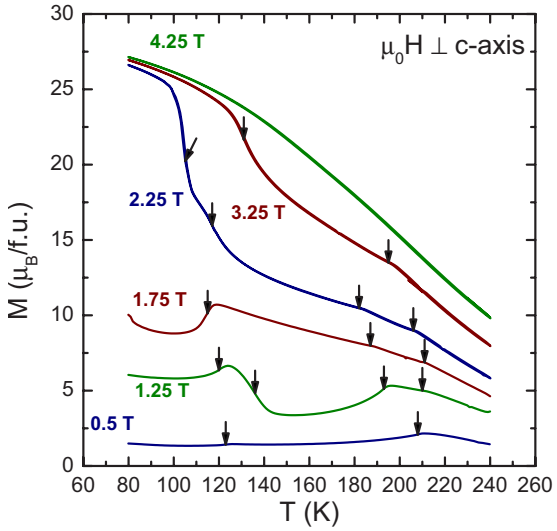

FIG. 5. (Color online) Magnetization as a function of (decreasing) temperature for fields ($\mu_0 H \perp c$ axis) between 0.5 and 4.5 T. The arrows indicate maxima in $\frac{\partial(MT)}{\partial T}$.

sitions. Based on the results of the previous section, where it was found that the peaks in the zero-field $\frac{\partial(\chi T)}{\partial T}$ appear very similar to the peaks in specific heat, we assume that peaks in $\frac{\partial(MT)}{\partial T}$ delineate magnetic phase boundaries. Anomalies determined from peaks in $\frac{\partial(MT)}{\partial T}$ are indicated by means of arrows in Fig. 5. Traces of $\frac{\partial(MT)}{\partial T}$ are shown in Fig. 6(c), as well as the positions of the peaks and their width, determined from half-width at half maximum on the steepest flank.

Detailed measurements of field-dependent magnetization at fixed temperatures were performed using a similar protocol as above. For each temperature, 5 and 10 K up to 220 K with 10 K steps, the sample was cooled in zero field, and the field was increased in steps of 0.025 T up to the highest measuring field. This field was chosen such that the magnetization appeared clearly saturated. After that, the field was increased up to above 4.5 T, without changing the temperature, and then the temperature was increased to above 250 K, at which temperature the field was removed. The results of these measurements are shown in Fig. 6(b) as a contour plot that displays the magnetization as a function of applied field and temperature.

As an often[52,56,57] applied criterion for transition fields, according to mean-field theory (see, e.g., Refs. 56 and 57), peaks in the differential susceptibility $\frac{\partial M}{\partial H}$, determined from magnetization isotherms, can be taken. Figure 6(a) shows several traces of $\frac{\partial M}{\partial H}$. The peaks and their width, determined from the half-width at half maximum on the steepest flank, are also indicated in Fig. 6(a). The differences between the peak positions indicated here and in Fig. 4 can be ascribed to differences in demagnetizing fields due to the different shapes of the samples.

Displayed together on top of the magnetization isotherms, in Fig. 6(b), the positions and the widths of the peaks obtained from both $\frac{\partial M}{\partial H}$ and from $\frac{\partial(MT)}{\partial T}$ appear to overlap. We therefore conclude that they indicate magnetic phase-

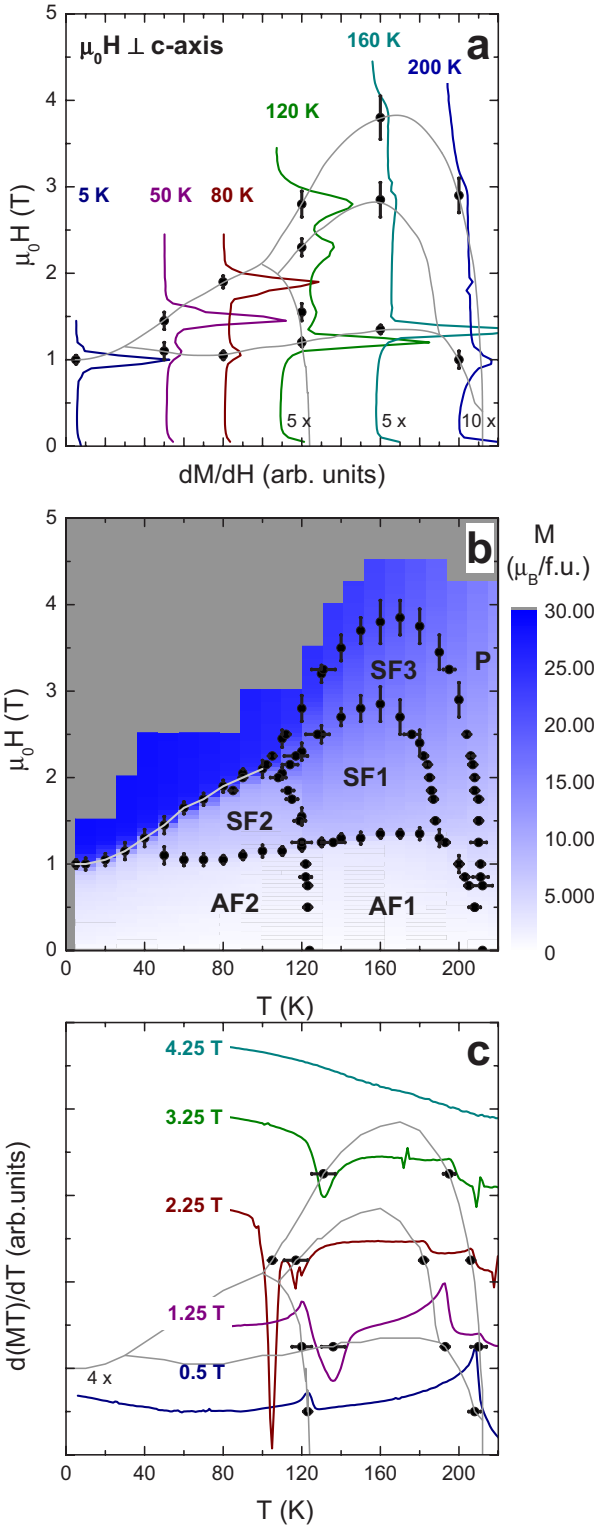

FIG. 6. (Color online) Magnetic phase diagram for Ce_2Fe_{17} obtained with the applied magnetic field $H \perp c$ axis. (a) Traces of $\frac{\partial M}{\partial H}$ obtained from field-dependent magnetization. Peaks and width of peaks are indicated. (b) Contour plot of magnetization $M(H,T)$ with peaks from (a) and (c) plotted on top. Labels are explained in the text. Dark gray indicates where no data were taken. (c) Traces of $\frac{\partial(MT)}{\partial T}$ obtained from temperature-dependent magnetization. Peaks and width of peaks are indicated.

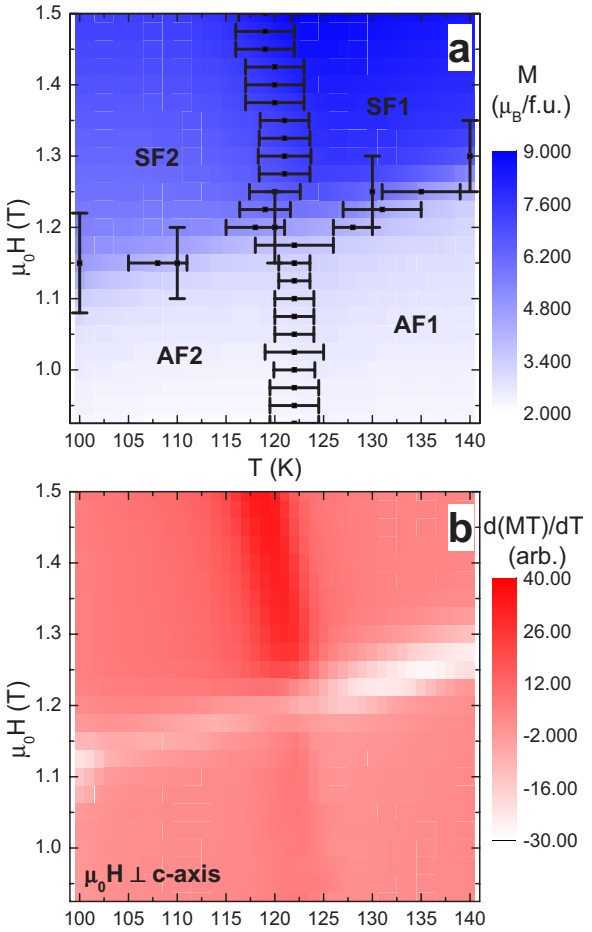

FIG. 7. (Color online) Detail of H-T phase diagram for $H \perp c$ axis. (a) Contour plot of magnetization $M(H,T)$ with peaks determined from $\frac{\partial(MT)}{\partial T}$ (horizontal bars) and peaks determined from $\frac{\partial M}{\partial H}$ (vertical bars) plotted on top. (b) Contour plot of $\frac{\partial(MT)}{\partial T}$ determined from (a).

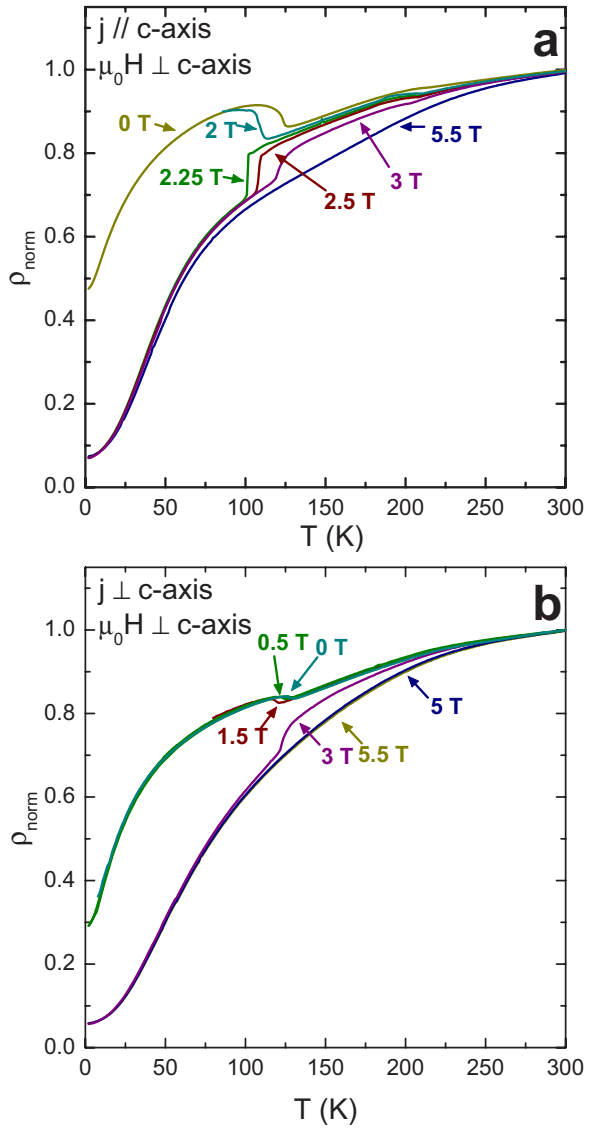

FIG. 8. (Color online) (a) Temperature-dependent normalized resistivity measured with $j \| c$ axis in different $H \perp c$ axis up to 5.5 T. (b) Same as (a) but for $j \perp c$ axis.

boundary lines, and thus outline a magnetic phase diagram. The phase-boundary line that is associated with clear hysteresis is drawn in gray. For the other phase-boundary lines, hysteresis was not observed. The labels will be discussed below.

To determine details of the apparent crossing of phase-boundary lines at about 120 K and in about 1 T, we performed a more detailed experiment. Temperature-dependent magnetization was measured upon cooling at 1 K steps between 140 and 100 K. Fields ranged between 1.5 and 0.925 T at 0.025 T steps. The results of the measurements are displayed in Fig. 7(a) as a contour plot that displays the magnetization as a function of applied field and temperature. In Fig. 7(b), we display the derivative $\frac{\partial(MT)}{\partial T}$ as a contour plot. The peak positions and their widths obtained from this experiment are included in Fig. 7(a) as well as peak positions and widths obtained from the magnetization isotherms in Fig. 6(b). From this it is clear that, within experimental resolution, there is a crossing of phase-boundary lines at ~122 K in ~1.2 T.

B. Resistivity

We determined temperature-dependent resistivity for the current j flowing$\| c$ axis as well as for $j \perp c$ axis in various applied fields $H \perp c$ axis up to 5.5 T. After the zero-field measurements, we performed measurements in applied fields. With the fragility of the material in mind, we measured, starting at 300 K, with both decreasing and increasing temperatures. In this way, we verified that the samples remained intact, which was obvious if, at a given temperature, the resistance measured upon heating was found to be the same as the resistance measured upon cooling. The measurements with $j \| c$ axis were performed at gradually lower fields, starting at 5.5 T. Down to 2.25 T, there was no significant change in the resistance determined with increasing or with decreasing temperatures.

The results are shown in Fig. 8(a) for $j \| c$ axis and in Fig. 8(b) for $j \perp c$ axis. For completeness, both Figs. 8(a) and 8(b)

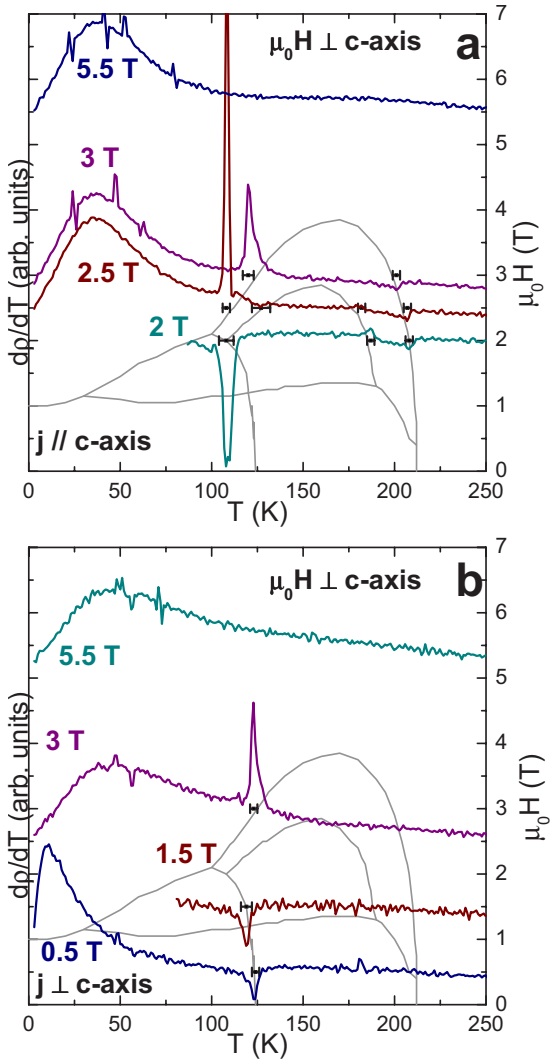

FIG. 9. (Color online) (a) Traces of $\frac{\partial\rho}{\partial T}$ for $j\|c$ axis, plotted on top of magnetic phase diagram for $H\perp c$ axis. (b) Same as (a) but for $j\perp c$ axis.

include the zero-field results from Fig. 2. Figures 9(a) and 9(b) show traces of $\frac{\partial\rho}{\partial T}$ plot over the phase diagram from Fig. 6. Also included in Fig. 9 are bars that indicate peak positions and widths in $\frac{\partial\rho}{\partial T}$. Note that the peaks in $\frac{\partial\rho}{\partial T}$ coincide well with the previously determined phase diagram.

The anomalous increase in resistivity with decreasing temperature, effects we ascribed above to the opening of an anisotropic superzone gap, observed in zero field for both current directions, occurs also in applied fields for both current directions. We observed it for fields of 2 T ($j\|c$ axis) and 1.5 and 0.5 T ($j\perp c$ axis). Note that in zero field and in 0.5 T, the crossed boundary lies between phases marked as AF1 and AF2, in Figs. 6 and 7, whereas for 1.5 and 2 T, the crossed boundary lies between the phases marked as SF1 and SF2.

Generally, for both employed current directions, the high-field resistivity at low temperatures is low, whereas for low fields it is high. The residual resistance ratio in 5.5 T, about 14 and 17 for $j\|c$ axis and $j\perp c$ axis, respectively, is much higher than in zero field. Since, as already indicated above, in Sec. IV, the resistivity for $j\perp c$ axis is hardly affected by superzone-gap effects, whereas its low-temperature resistivity is much lower in 5.5 T than in zero field, the superzone gap does not determine the large magnetoresistance, as was previously noted.[6] Assuming that the resistivity is determined as $\rho=\rho_0+\rho_{\text{lattice}}+\rho_{\text{mag}}$ and that the residual resistivity ρ_0 and the lattice contribution ρ_{lattice} are the same for the low-temperature AF2 or P phase, we consider the large magnetoresistance mainly caused by a strong change in magnetic scattering ρ_{mag}.

For $j\perp c$ axis, the anomalies associated with phase transitions are weaker than for $j\|c$ axis. The ordering transition between the paramagnetic phase P and AF1 (for 0.5 T) or between P and SF3 (for 1.5 and 3 T) is not observed as an anomaly for $j\perp c$ axis, nor is the transition between SF3 and SF1 (for 1.5 T). For $j\perp c$ axis, the transition between SF3 and P produces a clear anomaly. For $j\|c$ axis, weak anomalies mark the phase boundaries between P and SF3 (at 2, 2.5, and 3 T). For the purpose of this paper, we do not consider the "break" in resistivity around 175 K, for $j\|c$ axis in 5.5 T, resulting in a very broad "peak" in $\frac{\partial\rho}{\partial T}$ due to a phase transition.

Although the presented dataset is limited, we have been able to measure resistivity in every (H,T) phase in the phase diagram of Fig. 6. Our results indicate that the previously observed large magnetoresistance[6] is mainly due to a large (magnetic) scattering of conduction electrons in the low-temperature AF1 phase, which is strongly reduced in the field-induced P state. Here, the superzone gap is associated with the phase-boundary line that separates AF1 and SF1 (above 124 K) from AF2 and SF2.

VI. PURE Ce_2Fe_{17}: MAGNETIZATION RESULTS FOR $H\|c$ AXIS

In this section, we discuss magnetization for the field applied$\|c$ axis, resulting in an H-T magnetic phase diagram for this applied-field direction. As in Sec. V A, we used blocky samples for determining hysteresis behavior, and we used platelike samples for detailed magnetization measurements.

Figure 10 shows magnetization at various temperatures up to 145 K, measured on a blocky sample with both increasing and decreasing field strengths up to 5.5 T, applied$\|c$ axis, with a step of 0.1 T between measurements. With increasing fields, the magnetization at 2 K is small and increases slightly with increasing fields up to ~3.2 T. Then, around ~3.2 T, a metamagnetic transition takes place, followed by a second metamagnetic transition at ~3.9 T. Both these transitions show hysteresis. At 5.5 T, the magnetization is not saturated, and it reaches a value of ~26 μ_B/f.u. lower than the magnetization observed at 1.5 T for $H\perp c$ axis in Fig. 4. The lower-field metamagnetic transition occurs at temperatures below ~125 K, at which a zero-field transition occurs. The (increasing) field at which this metamagnetic transition occurs decreases slightly up to 80 K, and at the same time the hysteresis gradually becomes smaller. The field at which the higher-field transition occurs increases with increasing temperature, at least up to 80 K. The hysteresis associated

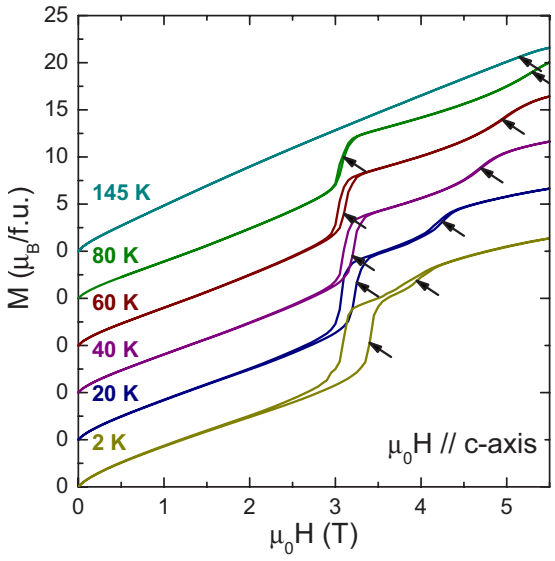

FIG. 10. (Color online) Magnetization at various temperatures for Ce_2Fe_{17} with the magnetic field $\mu_0 H \| c$ axis, measured with increasing and decreasing fields with steps of 0.1 T. For clarity, the curves have been offset with respect to one another. The black arrows indicate maxima in $\frac{\partial M}{\partial H}$ for increasing fields.

with this transition is observed at 20 K, but not at 40 K nor at higher temperatures. At 145 K, the magnetization increases smoothly, and without anomalies, until it approaches saturation near 5.5 T.

Figure 11 shows the field evolution of temperature-dependent magnetization, measured on a platelike sample, at temperatures between 240 and 60 K. A similar strategy as described above in Sec. V A was used. We measured upon cooling and at 60 K, increased the field up to 7 T, and heated the sample to ~240 K before we removed the field. In a field of 7 T, the magnetization increases uniformly with decreasing temperatures, without clear anomalies. In lower fields

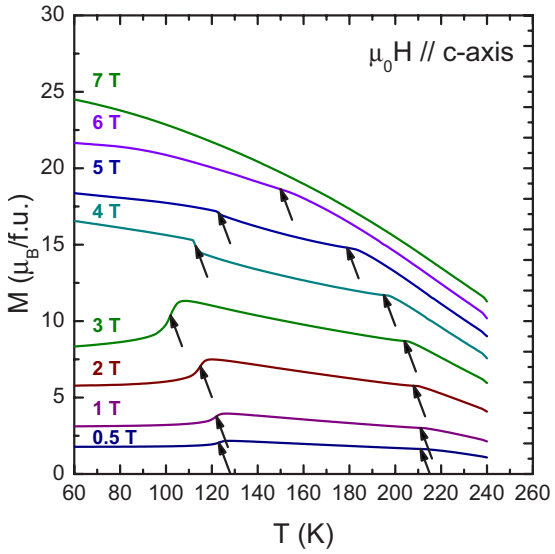

FIG. 11. (Color online) Magnetization as a function of (decreasing) temperature for fields ($\mu_0 H \| c$ axis) between 0.5 and 7 T. The arrows indicate maxima in $\frac{\partial (MT)}{\partial T}$.

multiple anomalies occur, associated with magnetic phase transitions. Based on the results of the previous sections, we assume that peaks in $\frac{\partial (MT)}{\partial T}$ in applied fields denote magnetic phase boundaries. Anomalies determined from peaks in $\frac{\partial (MT)}{\partial T}$ are indicated by means of arrows in Fig. 11. Traces of $\frac{\partial (MT)}{\partial T}$ are shown in Fig. 12(c), as well as the positions of the peaks and their width, determined from half-width at half maximum on the steepest flank.

Detailed measurements of field-dependent magnetization at fixed temperatures were performed using a similar protocol as above. For each temperature, 5 and 10 K up to 220 K with a 20 K step, the sample was cooled in zero field, and the field was increased in steps of 0.05 T up to 7 T. Then, the temperature was increased to above 250 K, at which temperature the field was removed. The results of these measurements are shown in Fig. 12(b) as a contour plot that displays the magnetization as a function of applied field and temperature.

The anomalies observed in these magnetization isotherms produced peaks in the derivatives $\frac{\partial M}{\partial H}$. Figure 12(a) shows several traces of $\frac{\partial M}{\partial H}$. The peaks and their width, determined from the half-width at half maximum on the steepest flank, are also indicated in Fig. 12(a). The differences between the peak positions indicated here and in Fig. 10 can be ascribed to differences in demagnetizing fields due to the different shapes of the samples.

As for Fig. 6, in Fig. 12(b) the positions and the widths of the peaks obtained from both $\frac{\partial M}{\partial H}$ and $\frac{\partial (MT)}{\partial T}$ overlap. We therefore conclude that they indicate magnetic phase boundary lines, and thus outline a magnetic phase diagram. Phase-boundary lines associated with hysteresis are indicated with gray lines. For the other phase-boundary lines, hysteresis was not observed. The labels will be discussed below.

Figure 13 shows details of the apparent splitting of phase-boundary lines at about 100 K and in about 3.2 T. Temperature-dependent magnetization was measured upon cooling at 1 K steps between 140 and 60 K. Fields ranged between 3.5 and 3.0 T at irregular intervals. The results of the measurements are displayed in Fig. 13(b) as a contour plot that displays the magnetization as a function of applied field and temperature. The contour plot shows field steps of 0.025 T; values for magnetization in fields between the measurement fields were obtained by interpolation. In Fig. 13(a), we display traces of the derivative $\frac{\partial (MT)}{\partial T}$. The peak positions and their widths obtained from this experiment are included in Fig. 13(a). Figure 13(b) also contains these peak positions and their widths, as well as widths obtained from the magnetization isotherms in Fig. 12(b). From this, it is clear that within experimental resolution, there is a splitting of phase-boundary lines at ~100 K in ~3.15 T.

VII. PURE Ce_2Fe_{17}: ANGLE-DEPENDENT MAGNETIZATION

Magnetization for fields applied at different angles θ with the c axis was measured on a platelike sample (mass <0.5 mg) mounted on a rotator. We measured over a range

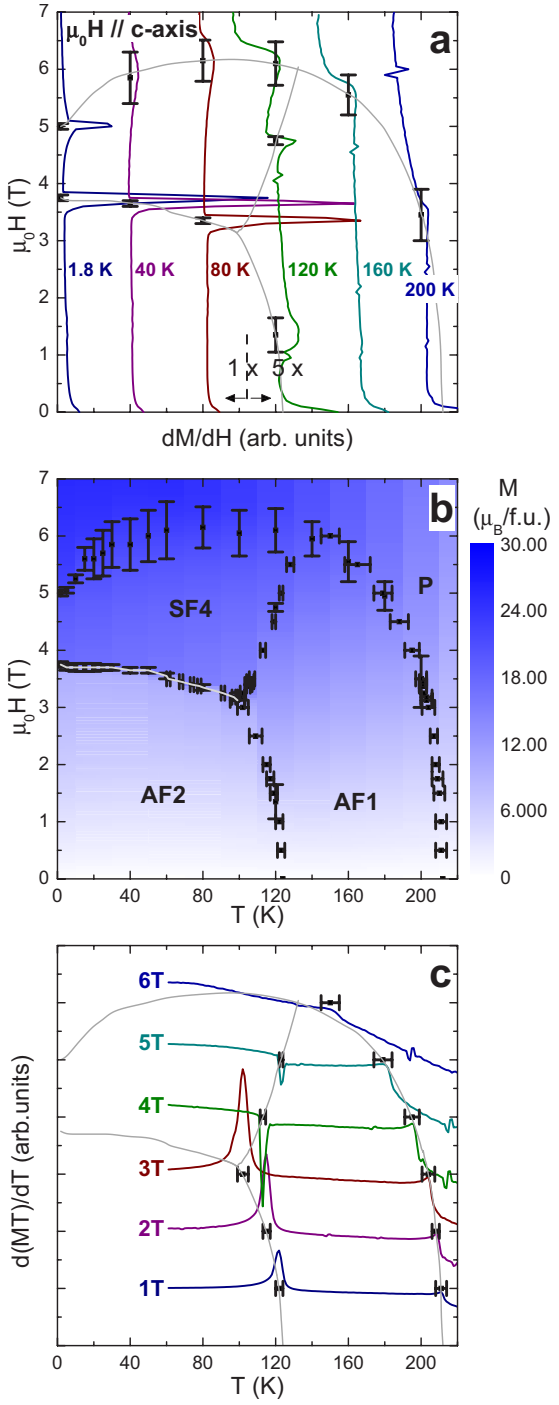

FIG. 12. (Color online) Magnetic phase diagram for Ce_2Fe_{17} obtained with the applied magnetic field $H\|c$ axis. (a) Traces of $\frac{\partial M}{\partial H}$ obtained from field-dependent magnetization. Peaks and width of peaks are indicated. (b) Contour plot of magnetization $M(H,T)$ with peaks from (a) and (c) plotted on top. Labels are explained in the text. (c) Traces of $\frac{\partial(MT)}{\partial T}$ obtained from temperature-dependent magnetization. Peaks and width of peaks are indicated.

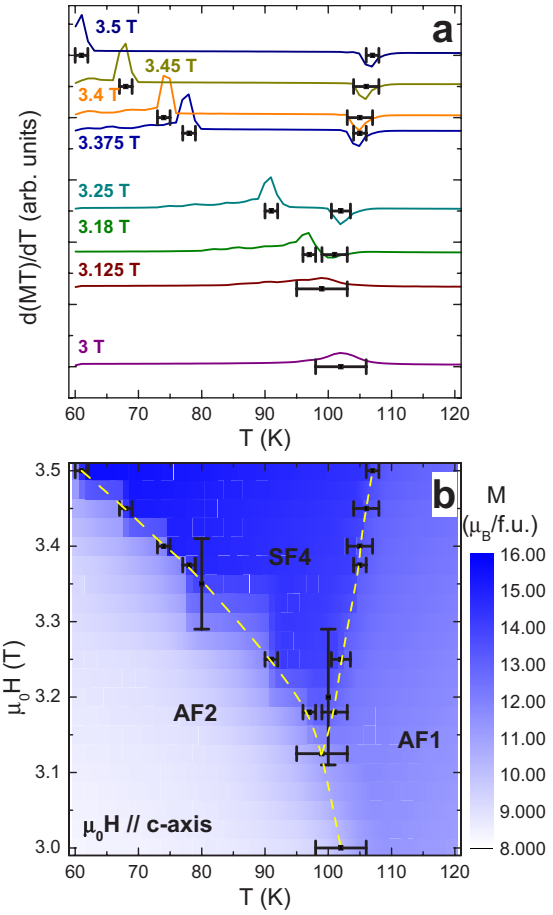

FIG. 13. (Color online) Detail of H-T phase diagram for $H\|c$ axis. (a) Traces of $\frac{\partial(MT)}{\partial T}$ obtained from temperature-dependent magnetization. Peaks and width of peaks are indicated as horizontal bars. (b) Contour plot of magnetization $M(H,T)$, obtained via interpolation, with peaks determined from $\frac{\partial(MT)}{\partial T}$ (horizontal bars) and peaks determined from $\frac{\partial M}{\partial H}$ (vertical bars) plotted on top.

of 130° with 5° steps, overshooting both $H\|c$ axis and $H\perp c$ axis. As above, to preserve the sample, we used a protocol. In zero field and at ~240 K, θ was set. Then, the sample was cooled to the measurement temperature, at which the magnetization was measured with increasing fields, every 0.05 T up to 7 T. After that, the sample was heated up, in 7 T, to ~240 K, at which temperature the field was removed, and a new θ was set.

The evolution of the magnetization, as θ is varied, for both $T=100$ K and $T=150$ K, is respectively shown in Figs. 14(a) and 14(b). Arrows indicate extrema found in $\frac{\partial M}{\partial H}$; note that some extrema are more clearly visible than others (cf. Figs. 4 and 10). For $H\|c$ axis, at 150 K, the magnetization increases smoothly up to about 5.5 T, where the magnetization starts to saturate. No s shapes marking phase transitions were observed for $H\|c$ axis. As θ increases, near 1–2 T an s shape appears that gradually develops into the steplike transition observed for $H\perp c$ axis. The transition that marks the field where the magnetization starts to saturate gradually decreases with increasing θ. Furthermore, with θ increasing above ~30°, an s shape appears at fields slightly lower than the saturation field.

Also at 100 K, with increasing θ, the field at which the magnetization starts to saturate gradually decreases. However, here it develops from a smooth, slightly s-shaped, nonhysteretic transition into a very sharp and hysteretic transi-

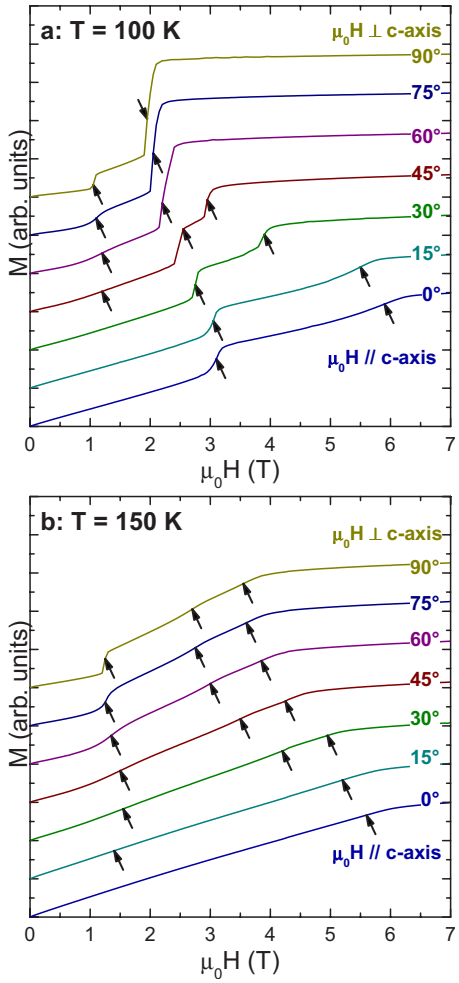

FIG. 14. (Color online) Evolution of magnetization isotherms (a) at 100 K and at (b) 150 K measured at angles with the c axis, with a 15° step, from $\|c$ axis to $\perp c$ axis. For clarity, the curves are offset with respect to one another. The arrows indicate extrema in $\frac{\partial M}{\partial H}$.

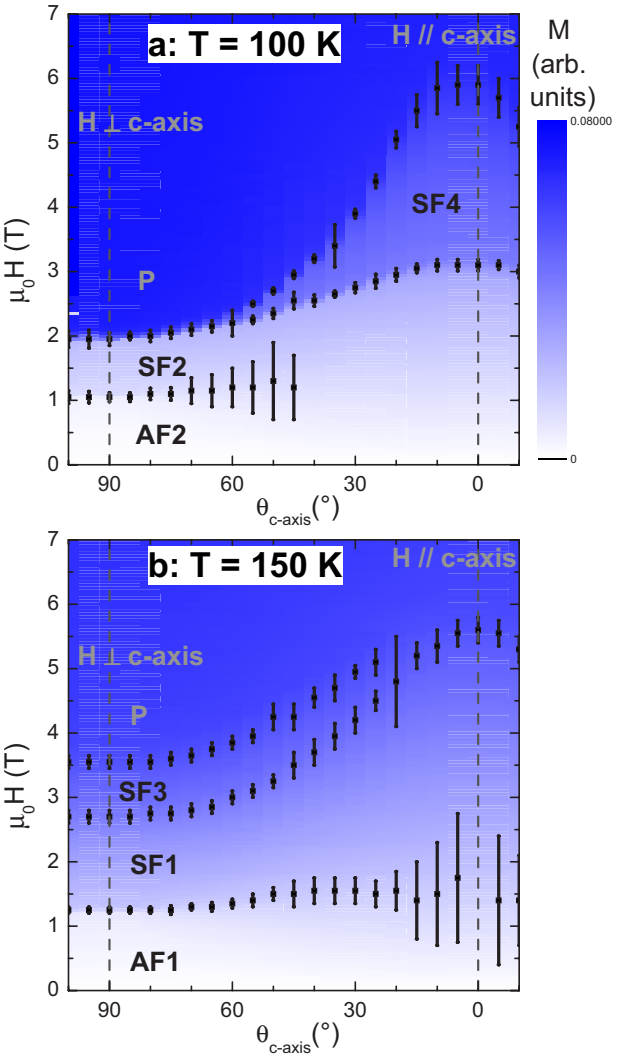

FIG. 15. (Color online) Magnetic phase diagrams determined at 100 and 150 K for fields applied at various angles θ with the c axis. (a) Contour plot of magnetization $M(H,\theta)$ at 100 K with peaks determined from $\frac{\partial M}{\partial H}$ (vertical bars) plotted on top. Labels are explained in the text. (b) Contour plot of magnetization $M(H,\theta)$ at 150 K with peaks determined from $\frac{\partial M}{\partial H}$ (vertical bars) plotted on top. Labels are explained in the text.

tion (see Figs. 10 and 4, respectively). With increasing θ, the sharp (and hysteretic) transition observed for $H\|c$ axis near 3 T shifts to a slightly lower field, and for $\theta > 45°$, appears to merge with the jumplike transition to saturation observed for $H \perp c$ axis. Furthermore, the steplike transition near 1.5 T, observed for $H \perp c$ axis, develops from an s shape that first appears for $\theta > 30°$.

Contour maps of $M(\theta,H)$ measured at 100 K (a) and 150 K (b), which are below and above the 125 K zero-field transition, respectively, are displayed in Fig. 15. Vertical bars denote peaks in $\frac{\partial M}{\partial H}$ and their widths obtained as above in Secs. V A and VI. Note that, especially for the less-visible transitions, the peak widths may be slightly underestimated (cf. Figs. 6 and 12). For Fig. 15(a), measured at 100 K for $H \perp c$ axis, transitions were found near ~1 T and near ~2 T, just as in Fig. 6. At the same temperature, for $H\|c$ axis, transitions were found near ~3 T and near ~5.7 T, just as in Fig. 12. Figure 15(b), measured at 150 K, compares similarly to Figs. 6 and 12. The labels are discussed in Sec. IX.

VIII. Ta-DOPED Ce_2Fe_{17}: MAGNETIZATION RESULTS FOR $H \perp c$ AXIS

In order to compare undoped Ce_2Fe_{17} to Ta-doped Ce_2Fe_{17}, we used the Ta-doped Ce_2Fe_{17} crystal with nominally 0.5% Ta, that was also used for the EPMA experiment. We chose to measure magnetization with the field $H \perp c$ axis because, as will become clear below, this is the most salient applied-field direction. Figure 16 shows a summary of these measurements. Figure 16(c) shows temperature-dependent magnetization curves, measured in 0.05, 0.5, 1, 1.5, 2, 3, 4, and 5 T, at (decreasing) temperatures between 250 and 5 K. In curves of $\frac{\partial(MT)}{\partial T}$ (not shown), extrema were found, which are indicated by arrows in Fig. 16(c). In fields of 3 T and higher, no sharp anomalies were observed, similar to undoped Ce_2Fe_{17} for $H \perp c$ axis in 4.25 T (see Fig. 5). In the

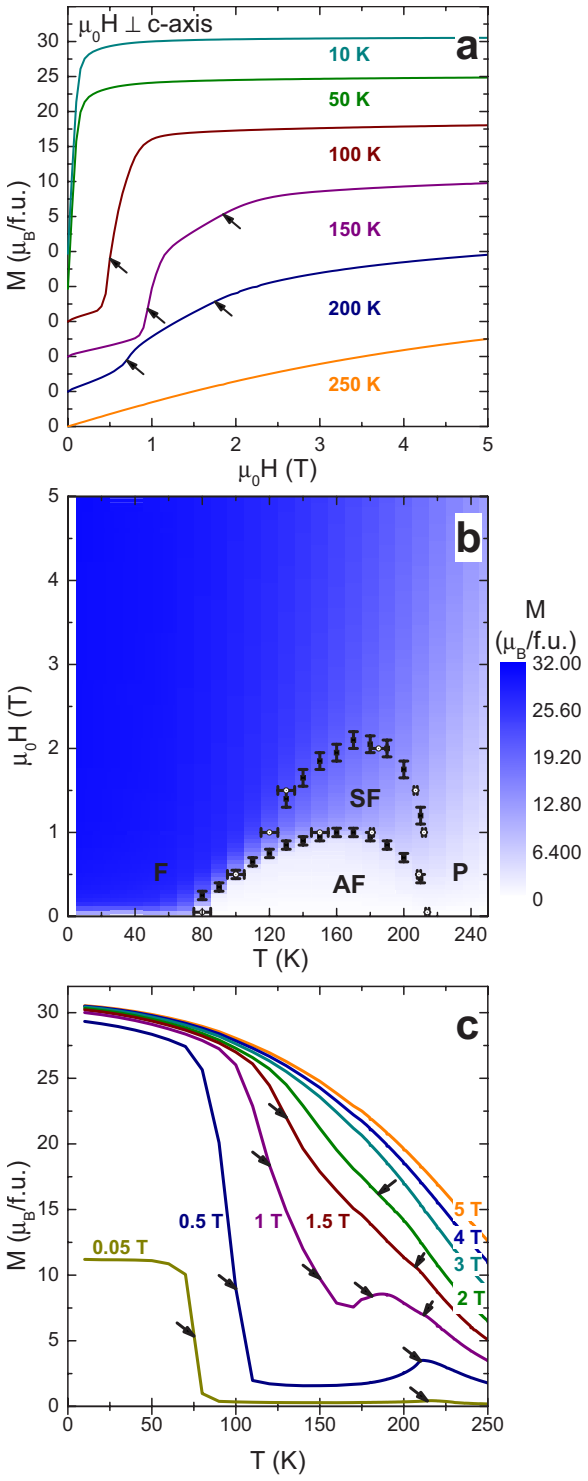

FIG. 16. (Color online) (a) Magnetization at various temperatures for Ta-doped Ce_2Fe_{17} with the magnetic field $\mu_0 H \perp c$ axis, measured with increasing fields with steps of 0.1 T. For clarity, the curves have been offset with respect to one another. The black arrows indicate maxima in $\frac{\partial M}{\partial H}$. (b) Contour plot of magnetization $M(H,T)$ with peaks from $\frac{\partial M}{\partial H}$ and $\frac{\partial (MT)}{\partial T}$ plotted on top. Labels are explained in the text. (c) Temperature-dependent magnetization in various fields up to 5 T. Arrows indicate phase-transition temperatures.

lower field of 2 T, anomalies appear, marking phase transitions. In contrast to undoped Ce_2Fe_{17}, a large magnetization is found below ~75 K in all applied fields of 0.05 T and higher, indicating that our sample of Ta-doped Ce_2Fe_{17} is ferromagnetic at low temperatures. The multiple anomalies in fields higher than 0.05 T, especially in 1 T, hint at a complex phase diagram. The low-field 0.05 T results are consistent with two ordering transitions, antiferromagnetic at $T_N = 214(1)$ and ferromagnetic at $T_0 = 75(5)$ K. Results of (increasing) field-dependent magnetization at various temperatures between 10 and 200 K are displayed in Fig. 16(a). At 10, and at 50 K, the magnetization shows ferromagnetic behavior, and no metamagnetic transitions are observed. The saturation magnetization of ~31 μ_B/f.u. at 10 K is in good agreement with results published for Ta-crucible grown Ce_2Fe_{17}.[22] At 100, 150, and 200 K, metamagnetic transitions were observed as maxima in $\frac{\partial M}{\partial H}$, at positions which are indicated by arrows. At 100 K, only one anomaly was observed, whereas at 150 and 200 K, two anomalies were observed, indicating the existence of a metamagnetic phase at these temperatures and consistent with the multiple anomalies found in temperature-dependent magnetization. Figure 16(b) shows a contour map of $M(H,T)$ and phase boundaries obtained from $\frac{\partial M}{\partial H}$ (vertical bars) and $\frac{\partial (MT)}{\partial T}$ (horizontal bars). The labels are analogous to those given for pure Ce_2Fe_{17}, but here is only one zero-field AF phase.

IX. DISCUSSION

The detailed study of the magnetic phase diagrams of undoped and of Ta-doped Ce_2Fe_{17} provides, due to the relationship between the samples, insight into the competition between ferro- and antiferromagnetic interactions in these compounds. In a magnetic phase diagram, one can find a phase-boundary line starting, in zero field, at the Néel temperature. It separates the paramagnetic phase from the magnetically ordered phase. Generally, its critical magnetic field strength increases with decreasing temperature.[56] However, for Ta-doped Ce_2Fe_{17}, the ground state is not antiferromagnetic but ferromagnetic. In such a case, the antiferromagnetic transition fields may form a "dome" in H-T, as predicted by Moriya and Usami in Ref. 32. Such a dome is indeed observed in the H-T phase diagram of Ta-doped Ce_2Fe_{17}, which in zero fields orders antiferromagnetically at the Néel temperature $T_N \sim 214$ K and ferromagnetically at $T_0 \sim 75$ K. Furthermore, besides the AF dome, there is an additional dome, enclosing a metamagnetic spin-flop-like phase (SF). This dome has a maximum field of ~2 T near 170 K. The zero-field behavior of the Ta-doped sample may be placed in the context of other studies. Prokhnenko *et al.*[23,58] determined pressure-dependent behavior of a polycrystalline ferromagnetic Ce_2Fe_{17} sample, which orders antiferromagnetically at $T_N \sim 214$ K and ferromagnetically at $T_0 \sim 97$ K. With increasing pressure, T_0 decreases strongly, whereas T_N decreases only slightly. From their data,[23] we estimate that a hydrostatic pressure of about 1 kbar causes T_0 in their sample to be reduced to about 75 K, whereas at this pressure T_N is barely affected. Based on these two characteristic temperatures, under 1 kbar the properties of their sample, in-

cluding its magnetic structure, may be comparable to the properties of our Ta-doped sample under ambient conditions. Note that, in the sample of Prokhnenko *et al.*, a further increase of pressure causes the ferromagnetic ground state to be replaced by an antiferromagnetic ground state, with a positively pressure dependent critical temperature T_t.

Undoped Ce_2Fe_{17} also orders antiferromagnetically at $T_N \sim 208$ K. Above $T_t \sim 124$ K, also the H-T phase diagram for $H \perp c$ axis Fig. 6 shows an AF dome. Besides this, there are two more domes, enclosing metamagnetic spin-flop-like phases, (SF1 and SF3). The dome enveloping SF3 has a maximum field of ~4 T at ~170 K. However, the boundary of this high-temperature SF3 dome does not go down to zero field at some lower temperature, instead it converges with another, low-temperature, dome which is connected to T_t at ~124 K, which is, as reported elsewhere in this volume,[59] associated with a crystallographic phase transition. This low-temperature dome also encloses a metamagnetic spin-flop-like phase, labeled SF2. The result is that undoped Ce_2Fe_{17} remains antiferromagnetic below T_t (AF2). Comparing our undoped sample to ferromagnetic Ce_2Fe_{17} of Prokhnenko *et al.*[23,58] under pressure at an estimated 20 kbar, T_t in their sample reaches ~120 K. Under these conditions, however, T_N is estimated to be reduced to ~175 K. Such discrepancies may be partially due to differences in effect on the unit cell of hydrostatic pressure as compared to doping.

As demonstrated in Fig. 7, there is a crossing of phase boundary lines at ~122 K in ~1.2 T. According to Landau,[60] for continuous phase transitions such crossings are only possible if the crossing phase-boundary lines represent different order parameters. Although from mean-field descriptions it may be concluded that spin-flop transitions are first order,[56] we observed no hysteresis in the measurements of magnetization around the phase-boundary line separating the low-field phases AF1 and AF2 from the spin-flop-like phases SF1 and SF2, respectively. The phase-boundary that starts at T_t in zero fields is characterized by a superzone-gap-like feature in electrical resistivity. The superzone-gap-like behavior was observed for the phase transition from AF1 to AF2, and between SF1 and SF2. We therefore assume that the field-dependent superzone-gap-like behavior is connected to the observed zero-field crystallographic phase transition.[59]

The low-temperature dome that starts at T_t in zero field ends in about 1 T at 0 K. The boundaries of the low-temperature dome indicated by a gray line in Fig. 6 are due to hysteretic phase transitions. The boundaries of the high-temperature dome do not show hysteresis. The high-temperature dome is associated with an antiferromagnetic phase transition, and the low-temperature dome with a crystallographic phase transition. According to Landau,[60] a convergence of two phase-boundary lines of continuous phase transitions may produce a line of first-order phase transitions, under certain conditions.[61] In this picture, the gray line of hysteretic first-order phase transitions constitutes a combined crystallographic and antiferromagnetic phase transition.

Now we turn to the H-T phase diagram $H \| c$ axis for undoped Ce_2Fe_{17} (Fig. 12). At the Néel temperature, a phase-boundary line between AF1 and P starts. It is connected to a phase boundary line enveloping SF4 and a phase-boundary line between SF4 and AF1. The boundary between SF4 and P becomes hysteretic below ~20 K. If the s-shape magnetization just below 140 K is due to a continuous phase transition, then this phase-boundary line may have a tricritical[56,57] point near 20 K (see Fig. 10).

Connected to T_t is a phase-boundary line, between AF1 and AF2, that is associated with a crystallographic phase transition;[59] this line is connected to the hysteretic phase-boundary line between AF2 and SF4 and to the phase-boundary line between AF1 and SF4. Obviously, the hysteretic phase-boundary line between AF2 and SF4 represents first-order phase transitions. Then, following thermodynamic arguments,[60,61] the phase-boundary line between AF1 and AF2 and the phase-boundary line between AF1 and SF4 may represent continuous phase transitions at this point.

Comparing the magnetization behavior near the T_t line in fields below ~2.5 T, it appears that the magnetization at lower temperatures is lower than that at higher temperatures. Thus, the crystallographic phase transition[59] affects the magnetic properties for this applied-field direction. The situation is different for higher fields, because at a given field above ~3.5 T, the magnetization in the low-temperature phase SF4 is higher than that in the neighboring phase AF1. This suggests that the phase-boundary line between AF1 and SF4 is associated with the occurrence of a low-temperature field-stabilized phase.

At 150 K, well above T_t, the antiferromagnetic phase transition is observed for both $H \| c$ axis and $H \perp c$ axis near 3.5 and 6 T, respectively, whereas spin-flop-like phase transitions are only observed for $H \| c$ axis. The angle-dependent magnetization experiment [Fig. 15(b)] shows how the antiferromagnetic transition and the transitions between AF1 and SF1 and between SF1 and SF3, respectively, evolve as the angle between the applied field and the c axis is changed. In simple cases,[56] spin-flop transitions are observed for weakly anisotropic antiferromagnets, when the field is applied parallel to the ordered moment direction. In this picture, the angle-dependent results measured at 150 K indicate that the moments in Ce_2Fe_{17} order in the plane perpendicular to the c axis. Moreover, the angle-dependent behavior of the antiferromagnetic phase-transition field, which is higher for $H \| c$ axis than for $H \perp c$ axis, is also indicative of a magnetic anisotropy in favor of the plane $\perp c$ axis. Also at 100 K, well below T_t, the angle dependence of the antiferromagnetic phase-transition field, higher for $H \| c$ axis than for $H \perp c$ axis, indicates a magnetic anisotropy in favor of the plane $\perp c$ axis. The presence of the nonhysteretic spin-flop-like transition between AF2 and SF2 for $H \perp c$ axis and its absence for $H \| c$ axis, are also an indication that at 100 K the ordered magnetic moments lie in the plane $\perp c$ axis. The angle-dependent magnetization furthermore indicates that SF4, observed for $H \| c$ axis, is not connected to any phase that can be observed for $H \perp c$ axis. Therefore, the angle-dependent results are consistent with the interpretations that the hysteretic AF2-SF4 phase-boundary line includes the crystallographic phase transition, and that the phase-boundary line enveloping SF4 is related to the magnetic anisotropy, as also observed at 150 K.

We think the H-T phase diagrams of Ta-doped Ce_2Fe_{17} and of undoped Ce_2Fe_{17} are manifestations of competing antiferromagnetic and ferromagnetic exchange interactions.

The occurrence of magnetic phase transitions in itinerant-electron systems with one type of ferromagnetism and one type of antiferromagnetism in competition has been treated theoretically by Moriya and Usami.[32] They constructed possible phase diagrams, one of which is very similar to the Ta-doped Ce_2Fe_{17} for $H \perp c$ axis. This predicted phase diagram has a low-temperature ferromagnetic state, an antiferromagnetic phase at intermediate temperatures, and a paramagnetic state at high temperatures. In nonzero applied fields, the antiferromagnetic phase is enveloped by a dome.

Although similar, the phase diagram for Ta-doped Ce_2Fe_{17} (Fig. 16) is more complex than the one described by Moriya and Usami, because here the AF dome shows another dome on top of it, indicated as SF. In the work of Moriya and Usami, calculations are made for two competing and interacting magnetic modes, a uniform magnetization M_0 and a staggered magnetization M_Q, for the competing ferromagnetic state with wave vector 0 and antiferromagnetic state with wave vector Q, respectively. The free energy was expanded up to the fourth order in these magnetic modes, without considering magnetic anisotropy. It therefore seems that the model can be adjusted by including higher-order terms in magnetization, by including magnetic anisotropy, or by introducing more than two competing types of exchange interactions. Although the isotropic Moriya-Usami model has not been extended with an in-plane easy-plane anisotropy, no in-plane anisotropy has been observed for Ce_2Fe_{17}, and easy-plane systems with moments confined to the easy plane are expected to behave similarly to isotropic systems. Higher-order terms in magnetization are not expected to qualitatively change the possible phase diagrams.[32] We think that an extension of the theory by possibly including more than two competing and interacting magnetic modes may result in a phase diagram similar to the one we observed for Ta-doped Ce_2Fe_{17}. This seems plausible in view of the complexity of the crystal structure with five different crystallographic sites. Moreover, electronic-structure calculations on related Y_2Fe_{17} produced different exchange interaction parameters of both antiferromagnetic and ferromagnetic types, between these sites.[12] For Al-doped Fe_3Ga_4, Duijn[62] described a similar *H-T* phase diagram in a similar manner. In such a picture, the phase SF is canted, with a nonzero magnetization, and moreover, is characterized by a, possibly additional, wave vector different from the zero-field wave vector. This could possibly be verified by a neutron-diffraction experiment.

In a similar way, the *H-T* phase diagram for undoped Ce_2Fe_{17} can be evaluated. Here, at temperatures above T_t, there exist, besides the zero-field phase AF1, two additional ordered phases (SF1 and SF3). If the introduction of an additional competing magnetization for Ta-doped Ce_2Fe_{17} holds, both SF1 and SF3 are canted, and even more modes M_Q are relevant here. Within the framework of the Moriya-Usami theory, a small amount of (Ta) dopant influences the competition of M_0 and relevant M_Q's and the number of relevant M_Q in the intermediate-temperature ordered state. As indicated in the introduction, the electronic density of states is probably strongly peaked near the Fermi surface, and therefore the electronic and magnetic properties are strongly dependent on volume, as was also found in pressure-dependent neutron-diffraction studies on ferromagnetic Ce_2Fe_{17}.[23] Different intermediate-temperature behaviors of Ta-doped Ce_2Fe_{17} and undoped Ce_2Fe_{17} are likely related to differences in (local) volume.

X. CONCLUSIONS

The magnetism of Ce_2Fe_{17}, earlier thought to be abnormal, may be explained as being due to competing ferro- and antiferromagnetism, and without emphasis on the intermediate valence properties of Ce. Instead, it is well described by a Moriya-Usami-type phenomenological theory, which in its unmodified form yields magnetic phase diagrams for systems with a competition between one antiferromagnetic and one ferromagnetic mode. Magnetic phase diagrams obtained for undoped Ce_2Fe_{17} indicate that the magnetic order is determined by the competition between multiple antiferromagnetic modes and a ferromagnetic mode. This competition and the resulting magnetic order are sensitive to minor changes in the crystallographic unit cell. A minor amount of Ta preferentially substitutes for Fe on one of the four Fe crystallographic sites and enlarges the unit-cell volume. This Ta doping influences both the competition and the number of competing magnetic modes and results in a ferromagnetic ground state.

Within the ordered state of undoped Ce_2Fe_{17}, as detailed elsewhere in this volume,[59] a doubling of the unit cell in the c direction takes place, which is due to a minor atomic displacement. Also, this crystallographic modification has a distinct effect on both the competition and the number of competing magnetic modes. Here, the resulting ground state is antiferromagnetic, and it may thus be said that the crystallographic phase transition stabilizes the antiferromagnetism. The sensitivity of the magnetism to Ta doping and to a minor displacive change in crystal structure is likely related to a strong sensitivity of electronic properties to small changes in (local atomic) volume, which in turn is consistent with a strongly peaked density of states near the Fermi level, as reported for the related compound Y_2Fe_{17}.

In conclusion, the present work indicates that the same mechanisms that determine the magnetic properties of R_2Fe_{17} compounds, the presence of both ferro- and antiferromagnetic exchange interactions, and lattice anomalies play a crucial role in determining the magnetism in Ce_2Fe_{17}.

ACKNOWLEDGMENTS

The authors are indebted to S. L. Bud'ko, R. W. McCallum, K. W. Dennis, J. Frederick, S. Jia, M. Angst, R. J. McQueeney, and A. I. Goldman. Work at the Ames Laboratory was supported by the Department of Energy–Basic Energy Sciences under Contract No. DE-AC02-07CH11358.

*Present address: Brookhaven National Laboratory, Upton, NY 11973, USA; yjanssen@bnl.gov
[1] K. H. J. Buschow, Rep. Prog. Phys. **54**, 1123 (1991).
[2] K. H. J. Buschow and J. S. van Wieringen, Phys. Status Solidi **42**, 231 (1970).
[3] K. H. J. Buschow, Rep. Prog. Phys. **40**, 1179 (1977).
[4] K. H. J. Buschow, J. Less-Common Met. **11**, 204 (1966).
[5] D. Givord and R. Lemaire, IEEE Trans. Magn. **MAG-10**, 109 (1974).
[6] Y. Janssen, H. Fujii, T. Ekino, K. Izawa, T. Suzuki, T. Fujita, and F. R. de Boer, Phys. Rev. B **56**, 13716 (1997).
[7] D. P. Kozlenko, V. P. Glazkov, B. N. Savenko, and V. I. Voronin, Eur. Phys. J. B **41**, 445 (2004).
[8] J. Kamarád, O. Prokhnenko, K. Prokeš, and Z. Arnold, J. Phys.: Condens. Matter **17**, S3069 (2005).
[9] O. Prokhnenko, J. Kamarád, K. Prokeš, Z. Arnold, and A. V. Andreev, Phys. Rev. Lett. **94**, 107201 (2005).
[10] R. Coehoorn, Phys. Rev. B **39**, 13072 (1989).
[11] D. Givord and R. Lemaire, *Proceedings of ICM 1973* (Nauka, Moscow, 1974), p. 492.
[12] R. F. Sabiryanov and S. S. Jaswal, Phys. Rev. B **57**, 7767 (1998).
[13] L. M. Sandratskii, Adv. Phys. **47**, 91 (1998).
[14] K. Knöpfle, L. M. Sandratskii, and J. Kübler, Phys. Rev. B **62**, 5564 (2000).
[15] M. Marsman and J. Hafner, Phys. Rev. B **66**, 224409 (2002).
[16] S. Shallcross, A. E. Kissavos, S. Sharma, and V. Meded, Phys. Rev. B **73**, 104443 (2006).
[17] R. Plumier and M. Sougi, *Proceedings of ICM 1973* (Nauka, Moscow, 1974), p. 487.
[18] K. Koyama, T. Goto, H. Fujii, N. Takeshita, N. Mori, H. Fukuda, and Y. Janssen, J. Phys. Soc. Jpn. **67**, 1879 (1998).
[19] K. Koyama, H. Fujii, T. Goto, H. Fukuda, and Y. Janssen, Physica B **294**, 168 (2001).
[20] F. Ishikawa, T. Goto, and H. Fujii, Physica B **329**, 657 (2003).
[21] Y. Makihara, H. Fujii, T. Fujiwara, K. Watanabe, K. Takahashi, K. K. Koyama, and M. Motokawa, Physica B **329**, 663 (2003).
[22] Y. Makihara, Y. Uwatoko, H. Matsuoka, M. Kosaka, H. Fukuda, and H. Fujii, J. Magn. Magn. Mater. **272**, 551 (2004).
[23] O. Prokhnenko, C. Ritter, Z. Arnold, O. Isnard, J. Kamarad, A. Pirogov, A. Teplykh, and A. Kuchin, J. Appl. Phys. **92**, 385 (2002).
[24] P. A. Teplykh, A. Pirogov, A. Kuchin, and A. Teplykh, Physica B **350**, e99 (2004).
[25] D. P. Middleton, S. R. Mishra, G. J. Long, O. A. Pringle, Z. Hu, W. B. Yelon, F. Grandjean, and K. H. J. Buschow, J. Appl. Phys. **78**, 5568 (1995).
[26] D. Hautot, G. J. Long, F. Grandjean, and O. Isnard, Phys. Rev. B **62**, 11731 (2000).
[27] Y. Janssen, M. Angst, K. W. Dennis, R. W. McCallum, and P. C. Canfield, J. Cryst. Growth **285**, 670 (2005).
[28] O. Isnard, S. Miraglia, D. Fruchart, C. Giorgetti, S. Pizzini, E. Dartyge, G. Krill, and J. P. Kappler, Phys. Rev. B **49**, 15692 (1994).
[29] O. Isnard, S. Miraglia, D. Fruchart, C. Giorgetti, E. Dartyge, and G. Krill, J. Phys.: Condens. Matter **8**, 2437 (1996).
[30] O. Isnard, S. Miraglia, C. Giorgetti, E. Dartyge, G. Krill, and D. Fruchart, J. Alloys Compd. **262-263**, 198 (1997).
[31] D. Vandormael, F. Grandjean, V. Briois, D. P. Middleton, K. H. J. Buschow, and G. J. Long, Phys. Rev. B **56**, 6100 (1997).
[32] T. Moriya and K. Usami, Solid State Commun. **23**, 935 (1977).
[33] P. C. Canfield and Z. Fisk, Philos. Mag. B **65**, 1117 (1992).
[34] P. C. Canfield and I. R. Fisher, J. Cryst. Growth **225**, 155 (2001).
[35] K. Koyama, H. Fujii, and P. C. Canfield, Physica B **226**, 363 (1996).
[36] L. H. Lewis, J. Y. Wang, and P. C. Canfield, J. Appl. Phys. **83**, 6843 (1998).
[37] Materials Preparation Center, Ames Laboratory US-DOE, Ames IA 50011, http://www.mpc.ameslab.gov
[38] H. Okamoto, *Desk Handbook Phase Diagrams for Binary Alloys* (ASM International, Materials Park, OH, 2000).
[39] T. C. Ozawa and S. J. Kang, J. Appl. Crystallogr. **37**, 679 (2004).
[40] G. Calestani, N. Magnani, A. Paoluzi, L. Pareti, and C. Rizzoli, Phys. Rev. B **68**, 054424 (2003).
[41] O. Isnard, S. Miraglia, J. L. Soubeyroux, D. Fruchart, and A. Stergiou, J. Less-Common Met. **162**, 273 (1990).
[42] R. D. Shannon, Acta Crystallogr., Sect. A: Cryst. Phys., Diffr., Theor. Gen. Crystallogr. **A32**, 751 (1976).
[43] E. Girt and Z. Altounian, Phys. Rev. B **57**, 5711 (1998).
[44] B. Saje, S. Kobe-Beseničar, Z. Samardžija, A. E. Platts, D. Kolar, and I. R. Harris, J. Magn. Magn. Mater. **146**, L251 (1995).
[45] D. H. Dennison, M. J. Tschetter, and K. A. Gschneidner, Jr., J. Less-Common Met. **10**, 108 (1966).
[46] Z. Arnold, F. Honda, G. Oomi, T. Eto, O. Prokhnenko, and J. Kamarad, J. Magn. Magn. Mater. **242**, 797 (2002).
[47] M. Ellerby, K. A. McEwen, E. Bauer, R. Hauser, and J. Jensen, Phys. Rev. B **61**, 6790 (2000).
[48] M. Ellerby, K. A. McEwen, and J. Jensen, Phys. Rev. B **57**, 8416 (1998).
[49] J. M. Ziman, *Electrons and Phonons: The Theory of Transport Phenomena in Solids* (Oxford University Press, London, 1963).
[50] H. Fukuda, Y. Janssen, H. Fujii, T. Ekino, and Y. Morii, J. Magn. Soc. Jpn. **23**, 108 (1999).
[51] R. A. Ribeiro, S. L. Bud'ko, and P. C. Canfield, J. Magn. Magn. Mater. **267**, 216 (2003).
[52] E. Morosan, S. L. Budko, P. C. Canfield, M. S. Torikachvili, and A. H. Lacerda, J. Magn. Magn. Mater. **277**, 298 (2004).
[53] M. Angst, A. Kreyssig, Y. Janssen, J.-W. Kim, L. Tan, D. Wermeille, Y. Mozharivskyj, A. Kracher, A. Goldman, and P. Canfield, Phys. Rev. B **72**, 174407 (2005).
[54] M. E. Fisher, Philos. Mag. **7**, 1731 (1962).
[55] W. P. Wolf and A. F. G. Wyatt, Phys. Rev. Lett. **13**, 368 (1964).
[56] L. J. de Jongh and A. R. Miedema, Adv. Phys. **23**, 1 (1974).
[57] E. Stryjewski and N. Giordano, Adv. Phys. **26**, 487 (1977).
[58] O. Prokhnenko, I. Goncharenko, Z. Arnold, and J. Kamarad, Physica B **350**, 63 (2004).
[59] A. Kreyssig, S. Chang, Y. Janssen, J. W. Kim, S. Nandi, J. Q. Yan, L. Tan, R. J. McQueeney, P. C. Canfield, and A. I. Goldman, following paper, Phys. Rev. B **76**, 054421 (2007).
[60] L. D. Landau, Zh. Eksp. Teor. Fiz. **7**, 19 (1937).
[61] S. K. Yip, T. Li, and P. Kumar, Phys. Rev. B **43**, 2742 (1991).
[62] H. G. M. Duijn, Ph.D. thesis, Universiteit van Amsterdam, Amsterdam, 2000.